Influence of Nanoscale Roughness on Wetting Behavior in Liquid/Liquid Systems

A Thesis
Presented to
The Academic Faculty

by

Joanna Wilhelmina Tsao

In Partial Fulfillment
of the Requirements for the Degree
Master of Science in Chemical & Biomolecular Engineering

School of Chemical & Biomolecular Engineering
Georgia Institute of Technology
December 2014

Influence of Nanoscale Roughness on Wetting Behavior in Liquid/Liquid Systems

Approved by:

Dr. Sven H Behrens, Advisor
School of Chemical & Biomolecular Engineering
Georgia Institute of Technology

Dr. Dennis Hess
School of Chemical & Biomolecular Engineering
Georgia Institute of Technology

Dr. Carson Meredith
School of Chemical & Biomolecular Engineering
Georgia Institute of Technology

Date Approved: 10 July 2014

ACKNOWLEDGEMENTS

First, I would like to thank my advisor, Dr. Sven Behrens, for his guidance and support throughout my graduate career. Both were essential in my growth as a researcher and I consider myself extremely fortunate to have such an excellent advisor.

I would also like to thank Dr. Carson Meredith and Dr. Dennis Hess, for being part of my committee and for their valuable suggestions regarding my work.

I am grateful for the members of the Behrens group: Hongzhi, Joohyung, Abiola, and Yi, for being great colleagues and helping me when I needed it.

Finally, I'd like to acknowledge my family and friends for all the ways they've enriched my life.

TABLE OF CONTENTS

LIST OF TABLES

LIST OF FIGURES

LIST OF SYMBOLS

γ	interfacial tension/surface energy
γ^{LW}	Lifshitz-van der Waals component of surface energy
γ^{AB}	Lewis acid-base component of surface energy
γ^{+}	electron acceptor parameter
γ^{-}	electron donor parameter
ΔG	change in free energy
ΔV_s	streaming potential
ε_0	vacuum permittivity
ε_r	relative permittivity/dielectric constant
ζ	zeta potential
η	liquid viscosity
θ	contact angle
κ	radius of curvature
κ_B	specific conductivity
ξ	viscous dissipation
ρ	density
τ	characteristic time
h	height
f_i	area fraction of droplet in contact with species i, in Cassie-Baxter wetting
F_c	capillary force
F_v	viscous force
g	gravitational acceleration
I	light intensity

l	unit length of the contact line
L	characteristic length
m	mass
p	statistical significance
P	pressure
r	radius of the wetted area
r_{corr}	correlation coefficient
r_W	ratio of the actual surface area to the projected surface area, Wenzel factor
R	droplet radius
R_s	radius of asperity
R_{sk}	skewness
U	streaming potential
U_{ls}	liquid velocity at the liquid/solid interface
v	velocity of the contact line
V	drop volume
W_{adh}	work of adhesion

LIST OF ABBREVIATIONS

AFM	atomic force microscopy
APTES	(3-aminopropyl)triethoxysilane
Bo	Bond number
Ca	capillary number
CV	coefficient of variance
EKA	electrokinetic analysis
ES-100	Eudragit S-100
HDT	hydrodynamic theory
IEP	isoelectric point
MKT	molecular kinetic theory
Re	Reynolds number
RICM	reflection interference contrast microscopy
rms	root mean square roughness
SEM	scanning electron microscopy
vOCG	van Oss-Chaudhury-Good
w/v	weight per volume
XPS	x-ray photoelectron microscopy

SUMMARY

Wetting behavior of fluid/fluid/solid systems, largely influenced by surface properties and interactions between the three phases, plays a big role in nature and in industrial applications

Traditionally, wetting studies have focused on liquid/vapor systems, especially the study of a sessile liquid droplet in air. Liquid/vapor systems can only probe the effects of surface properties and interactions between the solid and the wetting liquid. This type of characterization is inadequate for liquid/liquid systems, where surface wettability is additionally influenced by interactions between the two wetting liquids.

The present study is the first to examine the effects of nanoscale roughness on wetting behavior in liquid/liquid systems and the modulation of roughness effects by fluid properties and the wetting order. This study examines both equilibrium and dynamic wetting behavior in liquid/liquid systems using well characterized substrates.

Rough substrates were fabricated by coating glass substrates with nanometer sized polymer particles. Partial dissolution of the particles and molecular de-deposition of the polymer allowed for tuning of substrate roughness while retaining the original surface chemistry. The effectiveness of this fabrication technique was verified using electron microscopy and electrokinetic analysis. We examined the wetting behavior in three fluid/fluid systems: an air/water system, a decane/water system, and an octanol/water system. The oils were chosen based on their different polarities.

Equilibrium wetting behavior was determined using contact angle measurements. Results indicate that for all systems where the primary wetting fluid was a liquid, an increase of the surface roughness resulted in Cassie-Baxter wetting. How hydrophilic a surface appears with regard to a water/fluid interface depended on the polarity of that fluid. The octanol/water system provided the strongest evidence regarding the effect of wetting order: a transition from Wenzel to Cassie-Baxter wetting was only observed when water was the primary wetting liquid. The observed transition was confirmed using a modified Wenzel/Cassie-Baxter model.

The kinetics of droplet spreading was measured using high speed optical microscopy. After a droplet was placed on a solid surface, the motion of the contact line was imaged at a rate of 1000 fps. The wetted area was then extracted using custom Matlab® scripts. The spreading kinetics underwent a transition between two regimes: a visco-inertial regime and a slower spreading regime. Results indicated that surface roughness influenced spreading kinetics in both regimes. The overall spreading rate was always slower for rough surfaces than for smoother surfaces. In liquid/liquid systems, the duration of visco-inertial regime was dependent on the surface roughness as well; in general, it was shorter for smooth substrates compared to rough substrates. Increasing the viscosity of the non-aqueous fluid significantly increased the duration of the visco-inertial regime and decreased the overall spreading rate..

This study provides insight into the competitive wetting of solid surfaces relevant in many industrial applications such as oil recovery or inkjet printing, and may guide the development of improved wetting models in an area that currently lacks an adequate theoretical description.

CHAPTER 1

INTRODUCTION

An understanding of equilibrium and dynamic wetting behavior in fluid/fluid/solid systems is important for many industrial applications including microfluidic devices, self-cleaning surfaces, and oil recovery [1-11]. The role of nanoscale roughness, order of wetting, and polarity and viscosity of the hydrophobic fluid all contribute to the observed wetting behavior. For example, optimizing oil recovery requires facilitating the motion of a liquid/liquid/solid line across a typically rough solid, a crucial wetting scenario that is not well studied theoretically.

1.1 Equilibrium wetting behavior

The effect of surface roughness on equilibrium wetting behavior has been extensively studied in liquid/vapor systems [1, 12-16]. Most studies have focused on generating surfaces exhibiting extreme wetting behavior and examined the effects of hierarchical surface roughness or the combined effects of varying surface chemistry and topography.

Varying the surface roughness of substrates studied in liquid/vapor systems can be achieved through a variety of different methods, such as changing the height and spacing of micropillar arrays [17], using inherently rough surfaces [14], roughening smooth metal surfaces [13], or modifying inherently rough surfaces [18]. Most of the methods used to change surface roughness also change the surface chemistry, making it difficult to determine if the observed wetting behavior is exclusively due to roughness effects. In general, increasing the surface roughness decreases the surface affinity for water in air [12, 13, 15, 17]. It is important to note that the effect of surface roughness on the observed wetting behavior is system dependent. In liquid/vapor systems, the exact effect of surface roughness depends on the type of surface tested and whether the liquid phase is water or oil [6, 16, 17].

In liquid/liquid systems, the surface affinity for water and oil in a water/oil system becomes important in equilibrium wetting behavior; oleophilic surfaces in an oil/air system can be oleophobic in oil/water systems [4, 7, 11]. Studies examining roughness effects in non-polar oil/water systems have found that surface roughness amplifies the wetting behavior of the smooth surface [11, 19]. Very few studies have been conducted to examine the effects of surface roughness for intermediate wetting behavior ($30^o < \theta_{eq} < 150^o$), which can provide a better understanding of wetting behavior for many common systems.

1.2 Dynamic wetting behavior

The study of dynamic wetting behavior has largely been limited to liquid/vapor systems, particularly the spreading of water droplets in air on smooth surfaces [20]. The spreading of a liquid droplet on a solid surface can be divided several different regimes, as shown in **Figure 1.1**. When a liquid droplet contacts a solid surface, the initial spreading behavior can be described using the hydrodynamic theory (HDT), which can be divided into three parts: the viscous regime, the inertial regime, and the capillary regime. The viscous and inertial regimes are named for the predominant force opposing surface tension [21]. In the capillary regime, the dominant force opposing surface tension is the viscous force; the name was chosen to avoid confusion. After the speed of the contact line has decreased below a threshold value, the observed wetting behavior can be described using the molecular kinetic theory (MKT), where spreading is the result of liquid/solid interactions on a molecular scale.

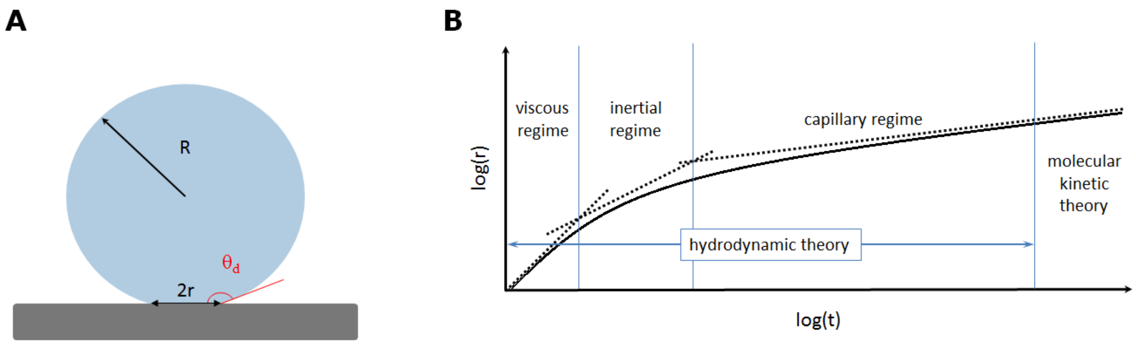

Figure 1.1. (A) A schematic of a water droplet spreading in air and (B) the sequence of spreading regimes associated with the hydrodynamic and molecular kinetic theories of droplet spreading

The duration of each regime and how liquid and surface properties influence spreading kinetics have been extensively studied in liquid/vapor systems [22]. There are still many general questions regarding spreading behavior in liquid/liquid systems. For example, HDT descriptions assume the viscosity of the surrounding fluid is negligible compared to the droplet viscosity (liquid/vapor systems), an assumption that is not valid in liquid/liquid systems, particularly the ones studied here. There are currently no systematic studies examining the initial spreading of droplets in liquid/liquid systems.

Surface chemistry or topography has been shown to affect spreading behavior only *after* the inertial regime in liquid/vapor and liquid/liquid systems [23-25]. While the hydrodynamic theory for the capillary regime and the molecular kinetic theory have both examined the effect of surface roughness on wetting behavior, most experimental studies have examined surfaces with simultaneously varied surface topography and chemistry, or have only varied the surface chemistry [17, 26]. When individual contributions from the two surface modifications could not be distinguished, differences in observed wetting behavior were only described in terms of the macroscopic equilibrium wettability of the substrate. While using that approximation has been effective when describing spreading kinetics on smooth, chemically heterogeneous surfaces [22], it is unknown if the assumption works for chemically homogeneous, rough surfaces.

In non-polar oil/water systems, the viscosity difference between the two reference liquids and the surface roughness have been shown to affect droplet spreading in within the framework of the molecular kinetic theory [19, 26]. However, the individual influence of liquid and solid surface properties in the first few spreading regimes and the effects of liquid polarity are still unknown.

1.3 Objective

In this study, we have extended the common characterization of surface wettability in to examine the combined effect of nanoscale roughness, type of reference fluid, and the order of wetting in a water/vapor system and two different oil/water systems.

In order to separate the effects of surface roughness from surface chemistry, substrates with varying surface roughness were generated using a solvent-based dissolution method. The success of the tuning procedure in changing surface topography while retaining the original surface chemistry was verified using several characterization techniques. Equilibrium surface wettability was characterized using contact angle measurements. Results from equilibrium studies were rationalized using a custom Wenzel/Cassie-Baxter model. Dynamic wetting behavior was studied for the first second after liquid/solid contact. The goal is to determine the effect of surface roughness on both equilibrium and dynamic wetting behavior and how roughness effects are modulated by fluid properties.

CHAPTER 2

SURFACE PREPARATION AND CHARACTERIZATION

The method used to generate macroscopic rough surfaces with varying surface roughness is described in **Figure 2.1** and is based on a previously reported method [27]. Rough substrates are generated by the irreversible adsorption of negatively charged nanoparticles, prepared via nanoprecipitation, onto positively functionalized glass substrates. Substrates are then immersed in solvent solutions where the solvent slowly extracts itself, leading to the molecular deposition of any dissolved particle material in a smooth film. The degree of smoothing is dependent on the solvent concentration. Two different sized particles were used to generate rough substrates to examine the influence of the starting particle size on wetting behavior.

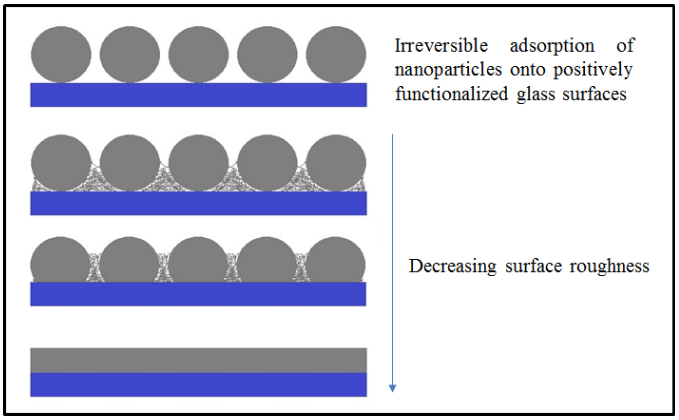

Figure 2.1. Scheme for the generating substrates with varying degrees of surface roughness

Using this method to smooth the substrates ensured that the surface was chemically homogeneous. Molecular re-adsoprtion was possible because the dissolving polymer had a high charge of opposite sign to the substrate charge and solvent evaporation slowly reversed the original polymer dissolution. Scanning electron microscopy (SEM) and atomic force microscopy (AFM) were used to characterize the topography of the generated substrates, and x-ray photoelectron spectroscopy (XPS) and electrokinetic analysis (EKA) were used to characterize the surface chemistry.

2.1 Fabrication of polymer particles

In order for the substrates to retain their original surface chemistry during the smoothing process, the particles must be chemically homogeneous. To achieve this, particles were made with Eudragit S-100 (Evonik Industries AG), a polymer with carboxyl and ester groups randomly distributed in an approximate 1:2 ratio throughout the polymer chain (**Figure 2.2**). Water-dispersible polymer particles usually have chargeable groups only on the surface, whether from the polymer initiator or a post-production surface treatment. The Eudragit S-100 (ES-100) particles used in this study were made from polymers with ionizable groups along the entire length of the polymer chain.

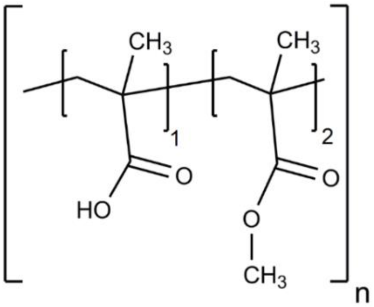

Figure 2.2. Chemical structure of Eudragit S-100 (ES-100)

Two different sized nanoparticles were prepared using nanoprecipitation. 0.5 g or 2 g ES-100 powder was first dissolved in 100 mL of reagent alcohol. The amount of polymer in the starting solvent controlled the final size of the particles [28, 29]. The alcohol solution was then quickly poured into 200 mL of pH 6 DI water stirred at 300 rpm. Since ES-100 is water-insoluble at this pH, the polymer precipitated out of solution in particle form. The alcohol and water solution was stirred constantly at 130^o C until all the alcohol evaporated. The particle solution was then filtered through a Grade 6 Whatman filter to remove any large aggregates that had formed. Size and zeta potential measurements were taken by dynamic and electrophoretic light scattering using Malvern Zetasizer Nanoseries ZS90 and the coefficient of variance (CV) was determined using a second order cumulant fit for the intensity autocorrelation function of the scattering signal. The 0.5% w/v solution made 60 nm particles with a CV of 17.6% and the 2% w/v solution made 195 nm particles with a CV of 24%.

2.2 Fabrication of rough substrates

Since ES-100 particles and the glass substrates are both negatively charged, substrates had to first be positively functionalized before particle adsorption. 22 mm square glass coverslips from VWR® were first washed with Alconox detergent solution, DI water, and acetone to remove any contaminants from the surface. The substrates were dried and immersed in a (3-aminopropyl)triethoxysilane (APTES) solution containing 50 mL water, 1 mL APTES, and 6 μm acetic acid for 15 minutes to positively functionalize the glass surface.

Clean substrates were rinsed twice in DI water, baked at 80^o C for 1 hr to covalently bond APTES to glass, then immersed in a 0.1 % w/v ES-100 solution. The ES-100 solution was prepared at pH 5.3. pH was adjusted with 10 mM HCl/NaOH. Immediately after substrates were immersed in solution, enough 3 M NaCl was added to reach a final concentration of 40 mM. Substrates were left in solution for 1.5 hrs for particle adsorption. The substrates were then rinsed three times in pH 5.3 water.

2.3 Tuning of surface roughness

Immediately after rinsing, substrates were immersed in a closed container filled with an aqueous acetone/water solution (containing 10% to 60% acetone) for at least 30 minutes. The containers were then opened to the atmosphere for 4-12 hrs. SEM images of 60 nm substrates indicated that extraction of acetone by evaporation in the fastest case (30 min closed container, 4 hrs room temperature) was slow enough to prevent precipitation of the polymer in the form of particles from the bulk solution.

Afterward, containers with 60 nm substrates were transferred to the fume hood until all the acetone had evaporated. Containers with 195 nm substrates were left to rest at room temperature until all of the acetone had evaporated. The larger particle size required a slower evaporation time step to prevent rapid precipitation of the polymer..

When all of the acetone evaporated from solution, substrates were rinsed in a 1 L solution of pH 5.3 water and left to dry for at least 24 hrs at room temperature before they were used.

2.4 Surface characterization

Several different techniques were used to characterize the prepared substrates and verify the change in surface topography was independent of surface chemistry. Scanning electron microscopy (SEM) and atomic force microscopy (AFM) were used to visualize the substrates and determine roughness parameters. Surface chemistry was determined using x-ray photoelectron spectroscopy (XPS) and electrokinetic analysis (EKA).

2.4.1 Scanning electron microscopy

SEM images were taken using a Zeiss Ultra 60 SEM at an accelerating voltage of 3-5 kV. Small sections of macroscopic surfaces were dried at room temperature and then attached to 45° aluminum stubs using carbon tape. Tilted stubs were used to better distinguish roughness features. Substrates were initially coated with gold prior to imaging but a carbon coating resulted in better images, as shown in the figure below (**Figure 2.3**).

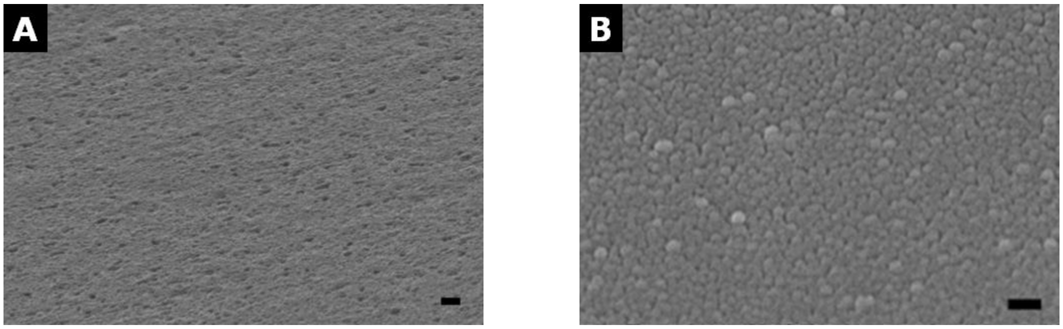

Figure 2.3. A rough substrate coated with (A) gold and (B) carbon. Scale bars represent 200 nm. Both images were taken using an accelerating voltage of 5 kV.

Substrates were coated with carbon using a Cressington 108A carbon coater. As can be seen in **Figure 3.4.2** and **Figure 3.4.3**, varying the percentage of acetone in the solvent solution effectively tuned the surface roughness for substrates generated using both 60 nm and 195 nm particles.

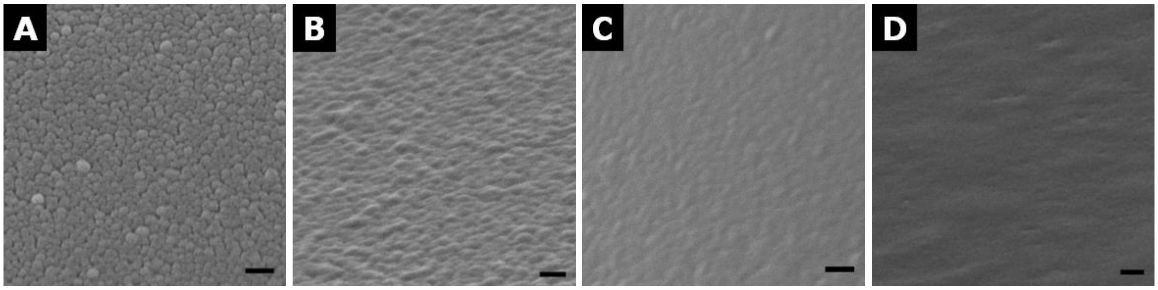

Figure 2.4. Glass substrates coated with 60 nm Eudragit S-100 nanoparticles treated with (A) 20%, (B) 35%, (C) 40%, and (D) 60% acetone solution. Scale bars represent 200 nm.

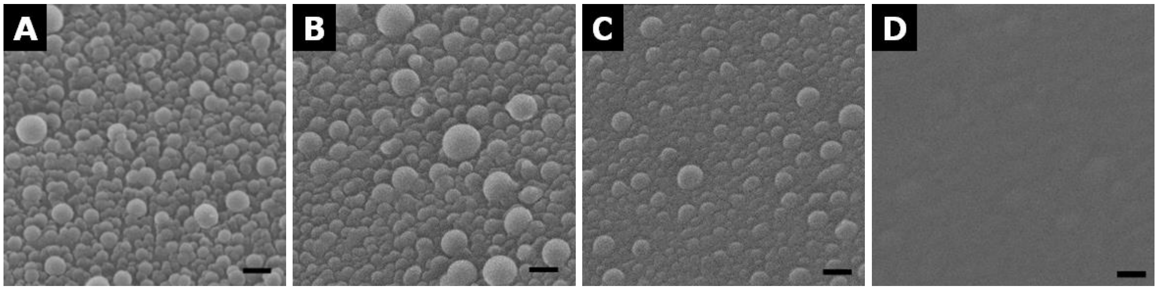

Figure 2.5. Glass substrates coated with 195 nm Eudragit S-100 nanoparticles treated with (A) 20%, (B) 30%, (C) 35%, and (D) 40% acetone solution. Scale bars represent 200 nm.

Qualitatively, the shape of surface asperities changes with increasing % acetone treatment. Rough substrates appear to have discrete surface asperities with "overhanging parts" or "re-entrant spaces". As the substrates are treated with increasingly concentrated acetone solutions, the interstitial space fills with dissolved polymer and the surface appears to have a more wavy appearance as it becomes smoother.

There are clear difference between substrates generated using 60 nm particles and 195 nm particles. Since 195 nm particle dispersions were much more polydisperse than 60 nm particle dispersions, roughness features on substrates coated with 195 nm particles were much less uniform than those generated using 60 nm particles. Particles from the 195 nm dispersion were not as tightly packed on the surface, which left visible gaps between the particles.

2.4.2 Atomic force microscopy

Scanning electron micrographs showed a qualitative change in substrate roughness with the acetone treatment. Quantitative measurements of surface roughness were measured with a Veeco Dimension 3100 atomic force microscope using Mikromasch silicon NSC14Al probes. Roughness parameters were determined using Gwyddion freeware. Typical AFM scans (scan areas of 10 µm x 10 µm) are shown in **Figure 2.6**.

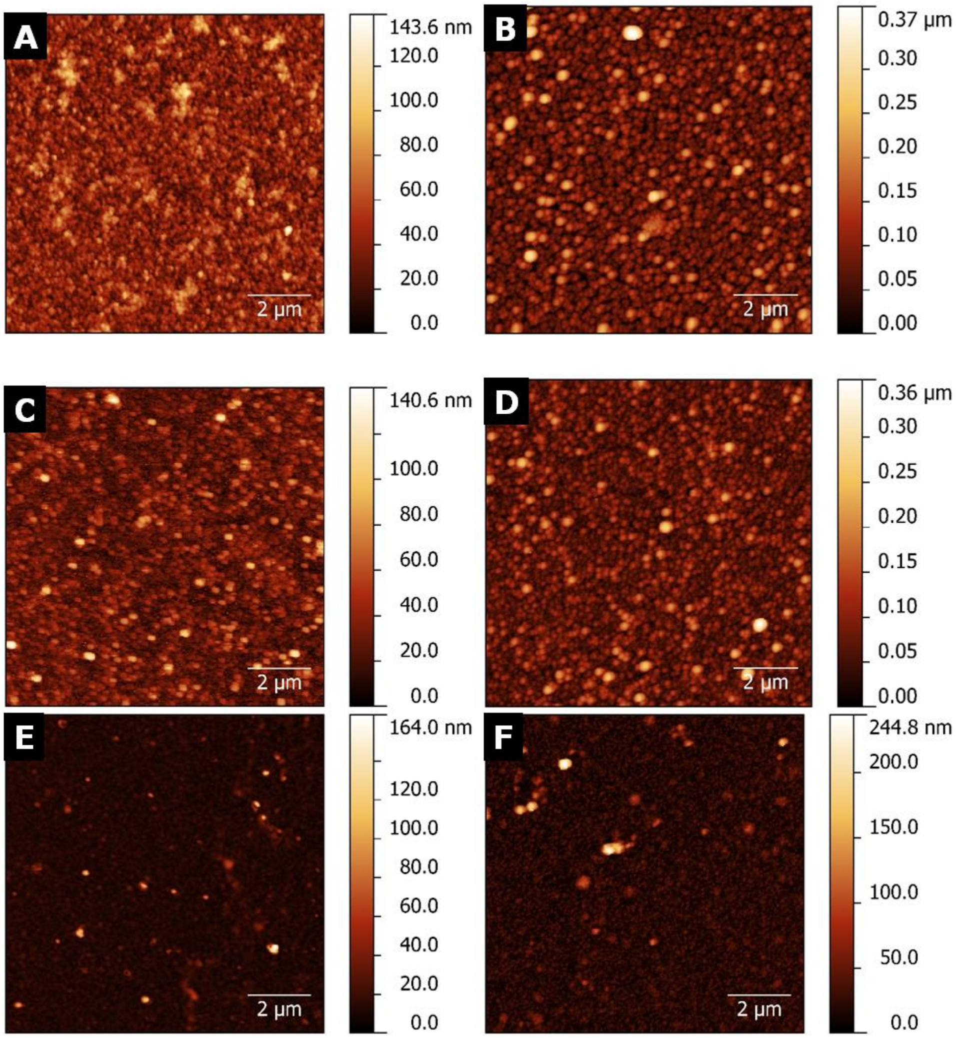

Figure 2.6. AFM images of 60 nm substrates treated with (A) 10 %, (C) 30%, and (E) 40% acetone solutions and 195 nm substrates treated with (B) 0%, (D) 20%, and (F) 40% acetone solutions

Roughness parameters were extracted from AFM scans of the substrate. The most common characterization of surface roughness measures the height of the asperities. The root mean square (rms) roughness describes the surface roughness using a statistical method and is more sensitive to deviations from the mean height than the average roughness [30, 31]. Rms measurements show that surface roughness decreases with increasing acetone treatment, seen in **Figure 2.7**.

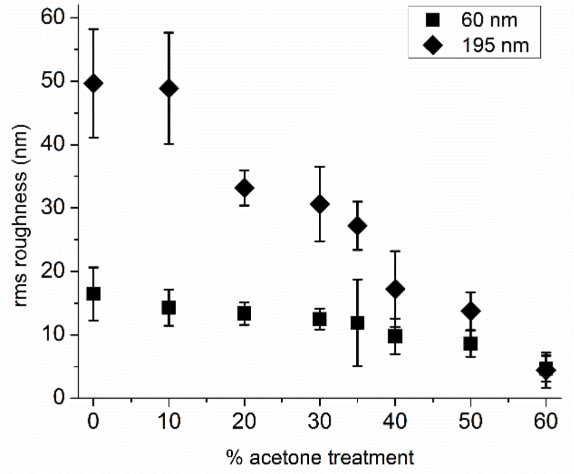

Figure 2.7. Atomic force microscopy measurements show that rms roughness decrease with increasing acetone treatment.

The roughest substrates generated using 195 nm particles have an rms roughness that is three times larger than substrates generated using 60 nm particles. This is expected based on the size difference between the two particle sizes. Despite the large difference in rms of untreated samples, 60 nm and 195 nm substrates treated with 60% acetone solution have similar rms roughness amplitudes.

The decrease in rms roughness with increasing acetone concentration confirms the effectiveness of our smoothing procedure. However, rms roughness cannot be used to completely describe how acetone concentration affects the substrates. It is obvious from

SEM images that the shape of the roughness features is changing with acetone treatment. The skewness (R_{sk}) of the surface was calculated to quantify changes in roughness shape.

Skewness is the third central moment of the height values collected from AFM and characterizes whether the measured roughness amplitude is due to the presence of valleys or peaks, as illustrated in **Figure 2.8**.

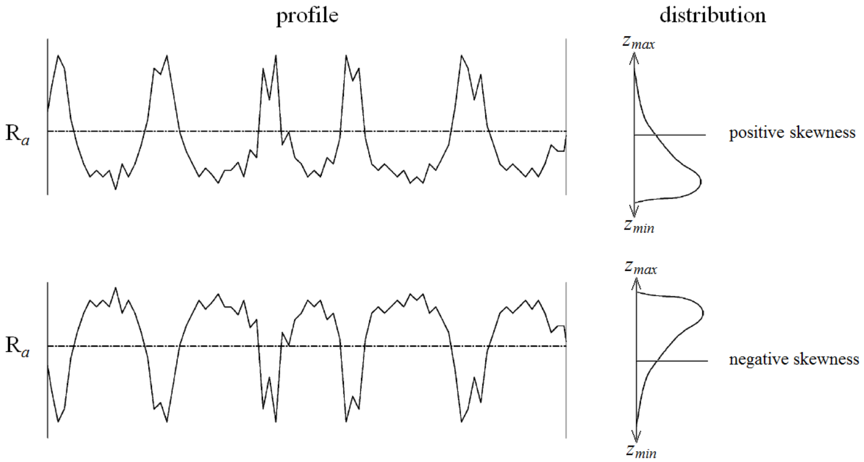

Figure 2.8. Height distribution of a rough surface and the corresponding skewness adapted from [31, 32]

Skewness characterizes the surface as having valleys (negative skewness) or peaks (positive skewness) and can differentiate between surfaces that may have the same roughness amplitude. An $R_{sk} > |1|$ indicates that the height distribution is far from symmetrical [31]. All substrates had an $R_{sk} > 1$ that increased with increasing acetone treatment (**Figure 2.9**).

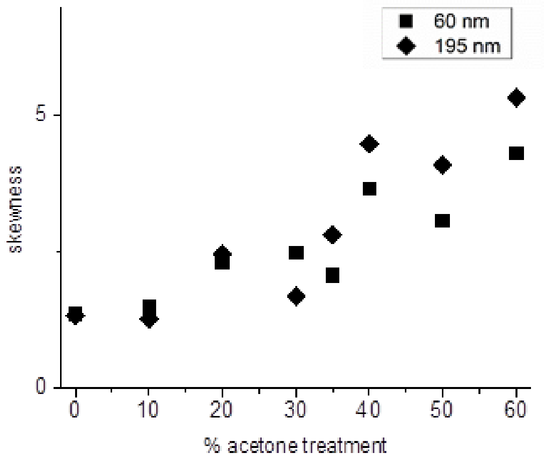

Figure 2.9. R_{sk} measurements for substrates generated using 60 nm and 195 nm substrates.

The relatively large % CV (above 10%) for both 60 nm and 195 nm particles may explain why the R_{sk} was always larger than 1. For a polydisperse solution of ES-100 particles adsorbed onto a solid surface, the larger particles will register as peaks on an otherwise flat surface. During the smoothing process, the solvent will dissolve a different percentage of particles on the same surface based on their size, exaggerating the difference between larger particles and smaller ones.

Another parameter that has been used to characterize surface roughness specific to wettability studies is the Wenzel factor r_W, which is the ratio of the actual surface area and the projected surface area (**Figure 2.10**). It is important to note that the actual surface area for rough surfaces determined using AFM will be an underestimate, particularly for surfaces generated using 60 nm substrates where the interstitial space is smaller than the tip radius.

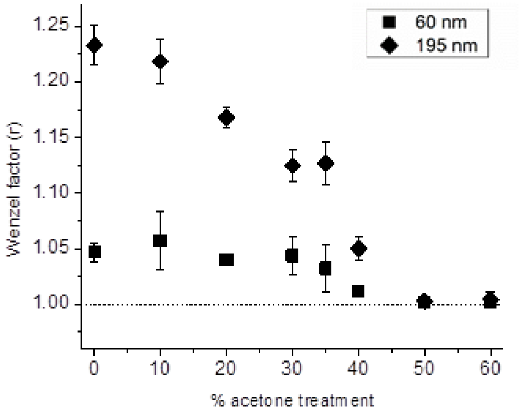

Figure 2.10. The ratio of the actual surface area and the projected surface area

Nonetheless, measurements of r_W indicate that the surface topography is changing during the acetone treatment. As expected, the effect is more pronounced in substrates generated using 195 nm particles. The Wenzel factor for the smoothest substrate generated using both sized particles is 1, despite a skewness > 5. The combined results suggest the large reported skewness is the result of only a few large particles and that the substrate is mostly flat.

2.4.3 X-ray photoelectron spectroscopy

XPS was used to characterize the substrates in order to confirm the substrates retained their original surface chemistry. Measurements were taken using a Thermo K-Alpha x-ray photoelectron spectrometer system using a beam strength of 0.1 eV over a scan area of 100 μm. The penetration depth of the electron beam was set to 3 – 5 nm, which is the minimum possible x-ray penetration depth of the system. Individual spectra for carbon (C1s) and nitrogen (N1s) were taken to probe the presence of ES-100 and APTES. The data were fit with Gaussian peaks in OriginPro® v 8.6. C1s scans are shown in **Figure 2.11** and were used to determine the different carbon bonds in the sample. The presence of COO bonds (288.5 eV) for both rough and smooth substrates confirm particle attachment and retention during the smoothing process. The binding energies associated with CO (~286.5 eV) and CN (~285 eV) bonding are very similar, so C1s spectra cannot determine if the polymer is completely coating the surface [33].

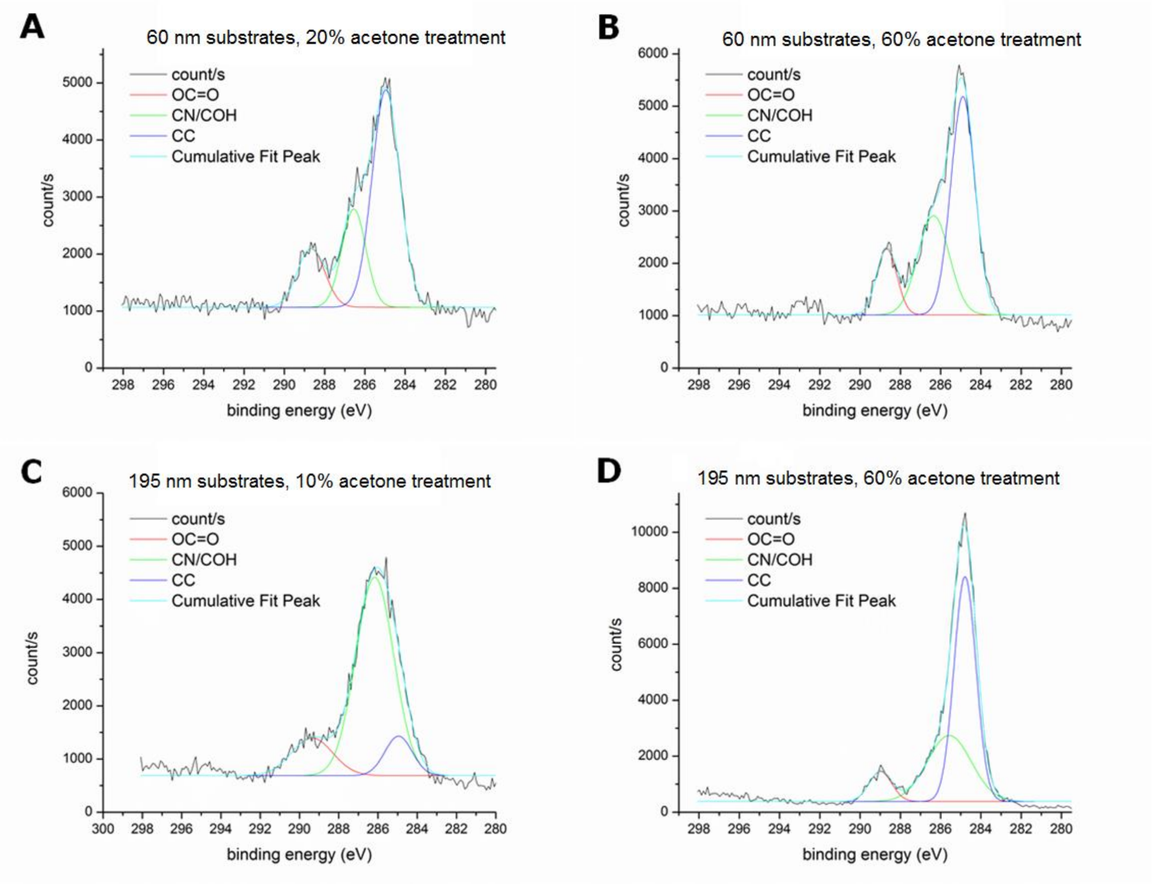

Figure 2.11. C1s spectra for substrates generated using 60 nm substrates after (A) 20% acetone and (B) 60% acetone treatment, and 195 nm substrates after (C) 10% acetone and (D) 60% acetone treatment.

N1s spectra were used as a more definitive way to verify the presence of APTES on the substrate surface since NH_2 bonds (~401 eV) are characteristic to the APTES molecule [34]. As shown in **Figure 2.12**, N1s spectra for rough substrates generated using 60 nm and 195 substrates show the presence of NH_2 bonds.

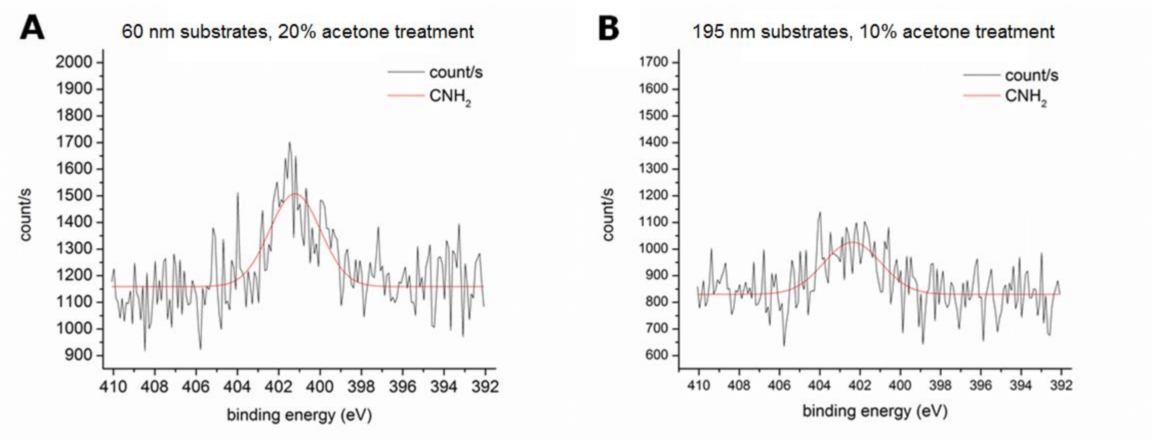

Figure 2.12. N1s spectra for substrates generated using (A) 60 nm after smoothing with 20% acetone and (B) 195 nm particles after smoothing with 10% acetone

By first appearance, the N1s spectra would indicate that the rough substrates are not completely covered with ES-100. However, at low % acetone treatment, any polymers that re-adsorbed to the exposed glass surface would form a film in the low nanometer range. Since the penetration depth of XPS was several nanometers, it is entirely possible that XPS spectra included elements beneath the polymer film.

N1s spectra for the smoothest substrates (60% acetone treatment) generated using 60nm and 195 nm particles XPS measurements do not indicate the presence of APTES, as seen in **Figure 2.13**. Taken with the presence of COO bonding on the same substrates (**Figure 2.11.B** and **Figure 2.11.D**), the results suggest the surface of the smoothest substrates were completely coated with a layer of ES-100.

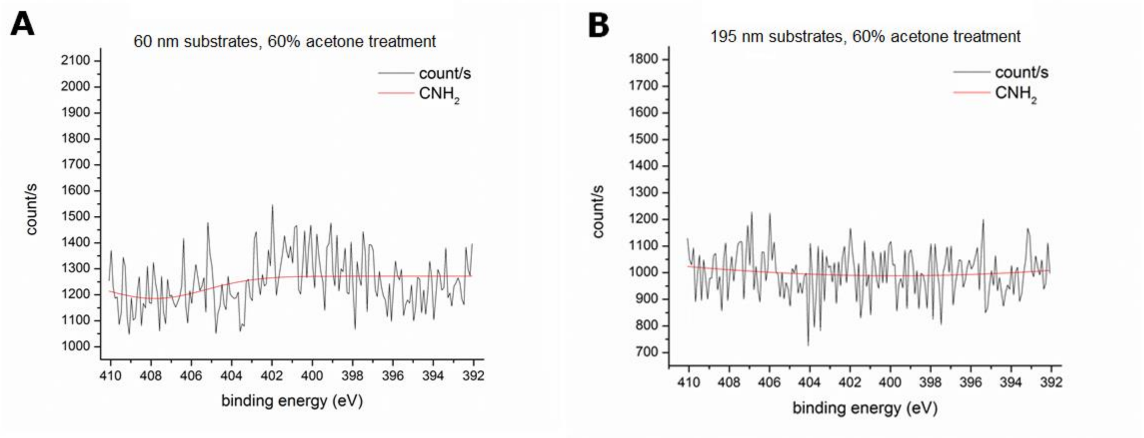

Figure 2.13. N1s spectra for substrates generated using (A) 60 nm and (B) 195 nm particles after smoothing with a 60% acetone solution. The lack of any signal associated with NH_2 bonding shows that no APTES is present on the sample surface.

XPS measurements verified that the smoothest substrates were completely coated with ES-100 polymer. However, XPS was unable to probe the surface chemistry of the rougher substrates without penetrating below the polymer coating.

2.4.4 Electrokinetic analysis

The use of electrokinetic analysis to characterize the surface chemistry of macroscopic substrates is based on the principle that surfaces tend to acquire electric charges in contact with water. The charged surface affects the ions in the aqueous solution, attracting an atmosphere of counter-ions to the surface, called the diffuse layer (**Figure 2.14**). The electrical potential at the edge of the hydrodynamic “shear plane” or “slip plane” close to the surface, called the zeta potential (ζ), is an approximation to the surface potential and indicates the degree of charging [35].

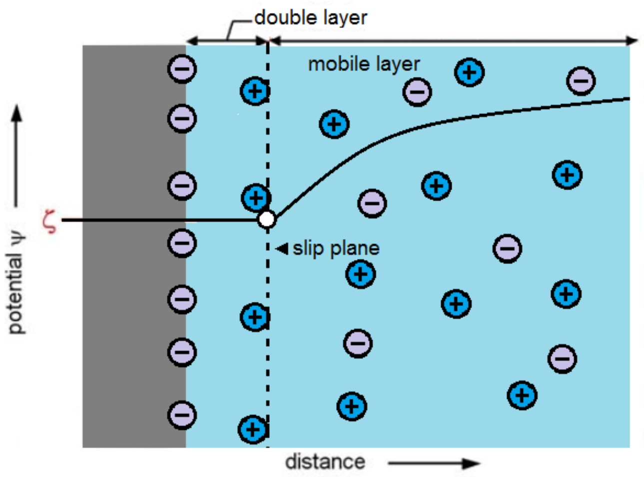

Figure 2.14. Schematic representation of the counter-ions surrounding a charged surface in water and the location of the slip plane and zeta potential

The zeta potential is not an absolute parameter; it can be influenced by the pH of the bulk solution, the type and concentration of electrolyte solution, surface topography, and the number of exposed chargeable groups [36]. By measuring the zeta potential of a surface while varying the pH and electrolyte solution, it is possible to determine the pH at which the surface carries no net charge, or the isoelectric point (IEP). Unlike the zeta potential, the IEP is dependent only on the type of chargeable group present on the surface and is therefore ideal for determining the surface chemistry of solid substrates. For example, APTES-coated surfaces will have an IEP of 8.5 due to the presence of NH groups [37, 38]. In order to prove that surface chemistry is retained throughout the entire smoothing process, the isoelectric point of all the modified substrates should be the same.

It is impossible to measure the zeta potential of macroscopic surfaces directly, so the zeta potential is calculated from the streaming potential. The streaming potential can be measured when pressure-driven flow forces an electrolyte solution through a gap such as a channel formed by two plates (**Figure 2.15)**. The pressure-driven flow entrains the counter-ion atmosphere of the charged surface, thereby setting up the electric current that leads to a potential difference along the flow direction. The potential difference, ΔV_s, is the streaming potential [39].

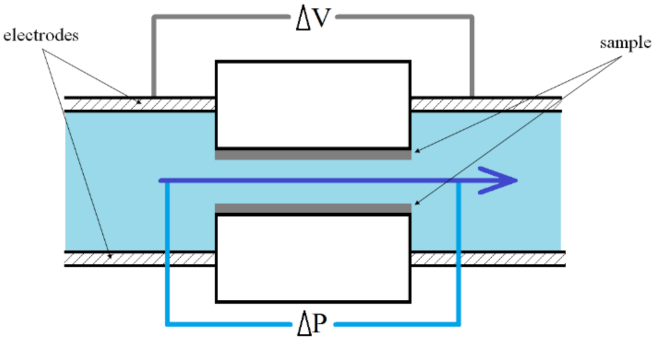

Figure 2.15. The device used to measure the streaming potential.

The zeta potential, ζ, is calculated from the streaming potential using the Helmholtz-Smoluchowski (H-S) equation, which is defined as:

$$\zeta = \frac{dV_s}{dP}\frac{\eta}{\varepsilon_0\varepsilon_r}\kappa_B \qquad \text{Eq. (1)}$$

where dV_s/dP is the slope of the streaming potential with respect to pressure, η is the liquid viscosity, ε_r is the relative permittivity, ε_0 is the vacuum permittivity, and κ_B is the specific conductivity of the electrolyte solution.

Zeta potential measurements were taken using an Anton-Paar Visio SurPASS Electrokinetic Analyzer. Zeta potential measurements of each substrate were taken at least four times using with a 1 mM NaCl solution at four different pH values ranging from 3 to 7.5 (**Figure 2.16**). As shown in **Figure 2.16**, the zeta potential for the measured pH values was dependent on the surface roughness, which is expected since the surface roughness influences the number of exposed chargeable groups [36]. The IEP was calculated using a cubic spline fit in Matlab® 2012 (**Figure 2.17**).

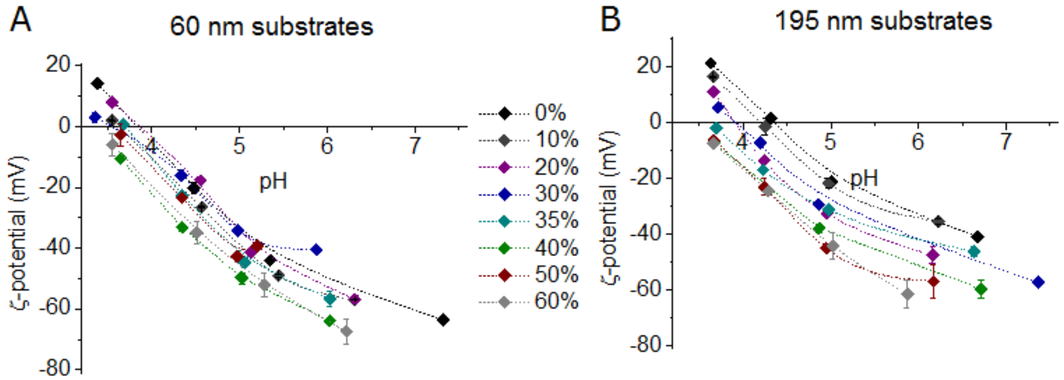

Figure 2.16. Zeta potential measurements taken in 1 mM NaCl solution for (A) 60 nm substrates and (B) 195 nm substrates.

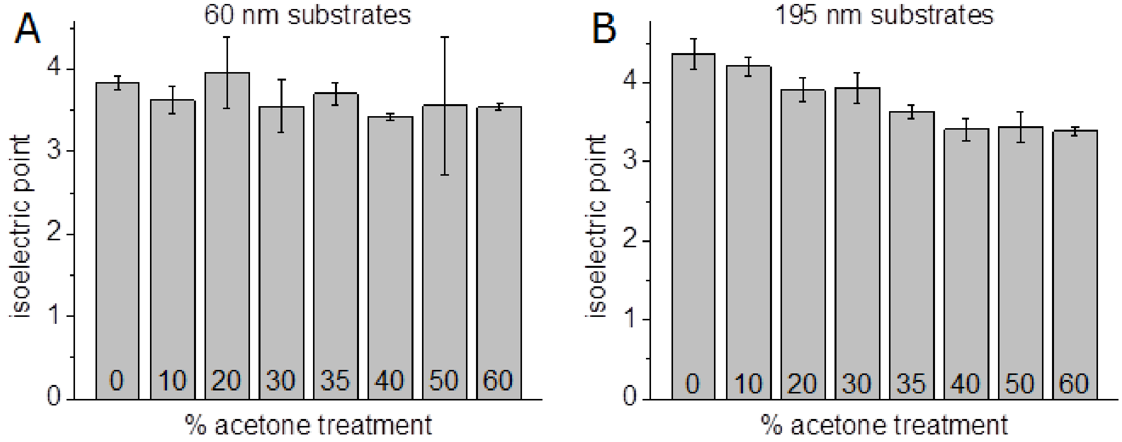

Figure 2.17. Calculated IEP values for substrates generated using (A) 60 nm substrates and (B) 195 nm substrates. Error bars represent the standard error of the calculation.

Statistical correlations for the dependence of the IEP on the % acetone solution used to smooth surface were determined with Pearson's *r*, using an r_{corr}- and a *p*- value. R_{corr} ranges from -1 (perfect negative correlation) to 1 (perfect positive correlation), and *p* can range from 0 to 1, and indicates the probability that the r_{corr} value could be observed by chance. In general, if $p < 0.05$, the correlation is considered statistically significant [40]. Statistical analysis showed no correlation for 60 nm substrates ($r_{corr} = -0.6183$, $p = 0.1023$). However, surface chemistry of substrates generated using 195 nm substrates was clearly dependent on the % acetone solution used to smooth the substrates (r_{corr} = -0.9522, p = 0.0003).

The IEP for 60 nm substrates is approximately the same for all acetone treatments, which indicates that the surface chemistry is insensitive to changes in surface topography. Zeta potential measurements of 195 nm substrates clearly show a correlation between the IEP and the degree of surface smoothing. The dependence is opposite of what is expected when the dissolution process fails. If the smoothing process was unsuccessful and surface chemistry was not retained throughout the process, the IEP would steadily increase with decreasing surface roughness. The opposite trend observed for 195 nm particle coatings indicates that the original particle deposition process was unsuccessful in this particular case; polymer particles did not completely cover the substrate. The calculated IEP is between that of APTES (pH 8.5) and a completely coated substrate (pH 3.5). The results suggest that rough substrates are chemically heterogeneous and remain so unless they have been immersed in solutions containing at least 35% acetone in water, when they are completely coated with ES-100. Any observed wetting behavior for 195 nm substrates was therefore due to the combined effect of surface chemistry and topography.

When measuring the zeta potential, it is useful to verify the general assumption that the solution represents an "indifferent electrolyte", or if specific binding of ions from solution contributes to surface charging. In the latter case, the IEP will show a clear dependence on the electrolyte concentration. If the charged surface groups have specific interactions with the electrolyte in solution, the IEP will be dependent on the electrolyte concentration [41].

Zeta potential measurements for the rough substrates (treated with 10% acetone solution) were taken with a NaCl solution at three different concentrations (1 mM, 10 mM, and 100 mM) at least three different pH values (**Figure 2.18**). Each measurement was taken at least four times. The IEP was calculated using a cubic spline fit in Matlab ® 2012 (**Figure 2.19**).

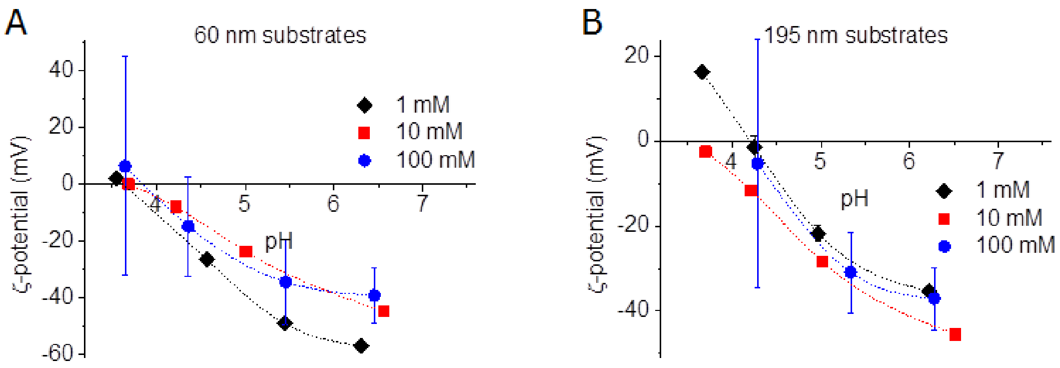

Figure 2.18. Zeta potential measurements taken in 1 mM, 10 mM, and 100 mM NaCl solutions for (A) 60 nm substrates and (B) 195 nm substrates

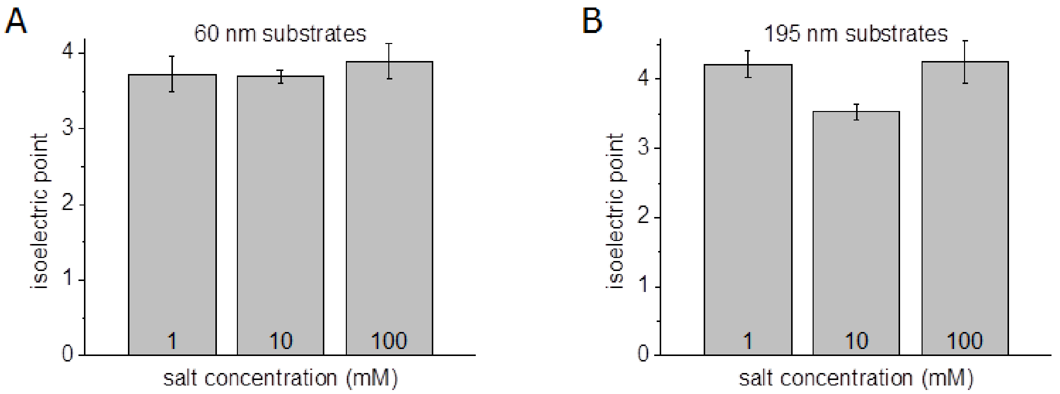

Figure 2.19. Calculated IEP values for substrates generated using (A) 60 nm substrates and (B) 195 nm substrates. Error bars represent the standard error of the calculation.

Substrates generated using 60 nm particles showed no dependence of the IEP on salt concentration (r_{corr} = 0.9723, p = 0.1501). The same behavior was observed with substrates generated using 195 nm particles ($r_{corr} = 0.4566$, $p = 0.6981$). From the results, we conclude that there is no specific ion adsorption on the substrate surface and the observed IEP at 1 mM NaCl solution represents the dissociation behavior of the surface groups.

Electrokinetic analysis was used to better characterize the surface chemistry of modified substrates. Results for substrates generated with 60 nm substrates confirm the assumption that smoothed substrates retain the same surface chemistry as untreated, rough substrates. Results from substrates generated using 195 nm substrates show that the surface chemistry changes with surface roughness.

2.5 Concluding remarks

We generated rough substrates through the irreversible adsorption of negatively charged nanoparticles onto positively functionalized glass surfaces. Substrates were smoothed using varying concentrations of a solvent solution using a method designed to retain the original surface chemistry. Surface characterization studies quantified the effect of the smoothing process on both the surface topography and surface chemistry. Surface topography studies showed that solvent and the concentrations chosen to smooth the substrates resulted in surfaces with varying surface roughness and roughness shape. Surface chemistry characterization confirmed the success of the smoothing procedure on substrates generated using 60 nm substrates.

The chemical heterogeneity of substrates generated using 195 nm nanoparticles was not with the smoothing procedure but with the particle deposition process. Scanning electron micrographs of rough substrates generated using the large particles showed that the particles were very polydisperse and there were visible gaps between the deposited particles where the underlying substrate was exposed. Substrates generated using 60 nm particles had a much higher packing density. It is possible that using less polydisperse 195 nm particles will result in chemically homogenous rough substrates.

CHAPTER 3

EQUILIBRIUM WETTING BEHAVIOR

3.1 Background

The standard method to quantitatively characterize surface wettability is by measuring the three phase contact angle, θ_{BAS}, as shown in **Figure 3.1**. In this study, surface wettability is characterized by surface hydrophilicity. A surface is considered hydrophilic when the water contact angle is below 90^o and super-hydrophilic when the water contact angle is below 10^o. A surface is considered hydrophobic when the water contact angle is above 90^o and super-hydrophobic when the water contact angle is greater than 150^o. For the purposes of this study, an "equiphilic" surface describes a surface where $85^o < \theta_{BAS} < 95^o$. The contact angle is most commonly defined as the angle between the droplet-liquid interfacial tension and the solid-droplet interfacial tension at the three phase contact line (θ_{BAS}). When the system is in equilibrium, θ_{BAS} is defined as the equilibrium contact angle, $\theta_{eq.}$

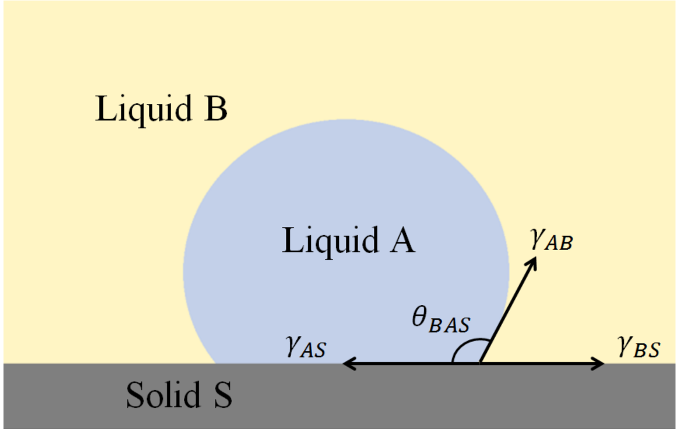

Figure 3.1. Schematic of contact angle and the three interfacial tensions in the system on an ideal surface

The equilibrium contact angle, θ_{eq}, relates the three interfacial tensions in the system: the droplet-solid interfacial tension, γ_{AS}, the liquid/solid interfacial tension, γ_{BS}, and the liquid/liquid interfacial tension, γ_{AB}, with the Young equation [42]:

$$\cos\theta_{eq} = \frac{\gamma_{BS} - \gamma_{AS}}{\gamma_{AB}} \qquad \text{Eq. (2)}$$

The Young equation assumes that the solid surface is rigid, smooth, and chemically and physically inert with respect to the surrounding fluids. In reality, most surfaces have some degree of roughness or chemical heterogeneity. Two theories are commonly used to correct for physical and/or chemical heterogeneities found on rigid surfaces.

3.1.1 Wenzel and Cassie-Baxter wetting regimes

In Wenzel wetting, surface heterogeneities amplify the wetting behavior of the ideal surface. It is most commonly applied to surfaces with physical heterogeneities, as shown in **Figure 3.2** [43].

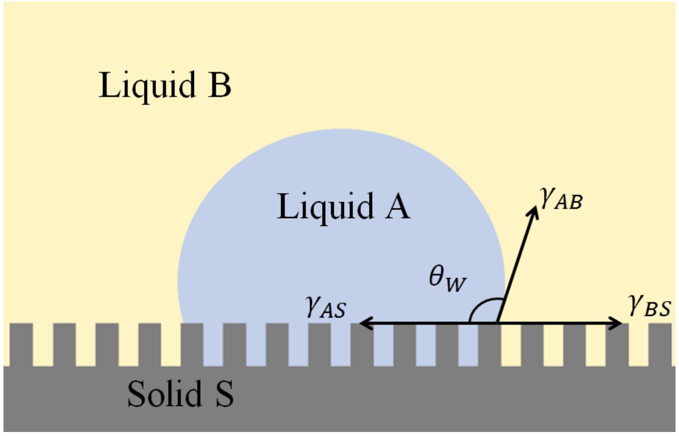

Figure 3.2. Schematic of a liquid droplet in the Wenzel wetting regime

The apparent equilibrium contact angle, θ_W, is related to the equilibrium contact angle, θ_{eq}, by describing the degree of surface roughness through the Wenzel factor, r_W:

$$\cos\theta_W = r_W \cos\theta_{eq} \qquad \text{Eq. (3)}$$

Since r_W is always ≥ 1 in the Wenzel regime, surface roughness will amplify the wetting behavior of a smooth surface, which will be termed the inherent wettability. An inherently hydrophilic surface will appear more hydrophilic as the degree of surface roughness increases, just as surface roughness will make an inherently hydrophobic surface appear more hydrophobic.

The Cassie-Baxter regime describes wetting behavior of a droplet on a chemically heterogeneous surface. There are many different scenarios that would result in a surface being considered chemically heterogeneous, such as a smooth surface with inconsistent surface chemistry or to the entrapment of the secondary fluid between the wetting droplet and the solid surface on a rough surface. An example of Cassie-Baxter wetting caused by the latter is seen in **Figure 3.3** [44].

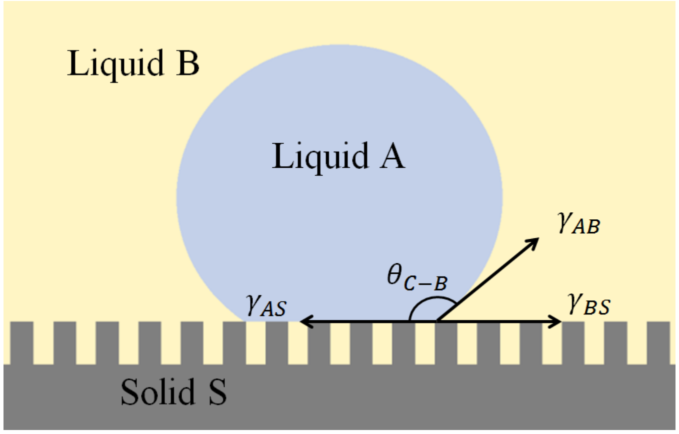

Figure 3.3. Schematic of a liquid droplet in the Cassie-Baxter wetting regime

For liquid/liquid systems in the Cassie-Baxter wetting regime, the area underneath the droplet is divided into two parts: the area fraction of the droplet in contact with the solid, f_1, and the area fraction of the droplet in contact with the surrounding liquid, f_2. The apparent equilibrium contact angle, $\theta_{C\text{-}B}$, is then defined as:

$$\cos\theta_{C-B} = f_1\cos\theta_1 - f_2 \qquad \text{Eq. (4)}$$

where θ_1 is the equilibrium contact angle of liquid A on the solid in liquid B. Unlike the Wenzel model, the Cassie-Baxter model has no roughness parameter, since surface roughness is taken into account when determining f_1 and f_2.

3.1.2 van Oss-Chaudhury-Good model for solid surface energy

According to the van Oss-Chaudhury-Good (vOCG) model, all condensed phases (i.e. liquids and solids) have a specific surface energy, γ, composed of a Lifshitz-van der Waals component, γ^{LW}, and a Lewis acid-base component, γ^{AB} [45, 46]. The surface energy is the sum of the two components:

$$\gamma = \gamma^{LW} + \gamma^{AB} \qquad \text{Eq. (5)}$$

The Lewis acid-base component is the result of contributions from an electron acceptor parameter, γ^+, and an electron donor parameter, γ^-:

$$\gamma^{AB} = 2\sqrt{\gamma^+\gamma^-} \qquad \text{Eq. (6)}$$

The interfacial tension between two condensed phases (γ_{12}) is then given by:

$$\gamma_{12} = (\sqrt{\gamma_1^{LW}} - \sqrt{\gamma_2^{LW}})^2 + 2(\sqrt{\gamma_1^+} - \sqrt{\gamma_2^-})\,(\sqrt{\gamma_1^-} - \sqrt{\gamma_2^+}) \qquad \text{Eq. (7)}$$

Since the change of free energy upon bringing these two phases into contact, ΔG_{12} is the negative of the work of adhesion, W_{adh}. ΔG_{LS} can be related to the liquid and solid surface energies (γ_L and γ_S, respectively) via [47-50]:

$$\Delta G_{LS} = -W_{adh} = \gamma_{LS} - \gamma_L - \gamma_S \qquad \text{Eq. (8a)}$$

$$\Delta G_{LS} = \Delta G_{LS}^{LW} + \Delta G_{LS}^{AB} = -2\sqrt{\gamma_L^{LW}\gamma_S^{LW}} - 2(\sqrt{\gamma_L^{+}\gamma_S^{-}} + \sqrt{\gamma_L^{-}\gamma_S^{+}}) \qquad \text{Eq. (8b)}$$

where ΔG_{LS}^{LW} and ΔG_{LS}^{AB} represent the change in free energy due to van der Waals and polar interactions, respectively. The change in free energy associated with liquid/solid adhesion can also be written as a function of the liquid/solid contact angle, θ_{eq}:

$$-\Delta G_{SL} = \gamma_L(1 + \cos\theta_{eq}) \qquad \text{Eq. (9)}$$

also known as the Young-Dupré equation [51]. Substituting **Equation 9** into **Equation 8**, the solid surface energy components (γ^{LW}, γ^{+}, and γ^{-}) can be calculated:

$$(1 + \cos\theta_{eq})\gamma_L = 2(\sqrt{\gamma_S^{LW}\gamma_L^{LW}} + \sqrt{\gamma_S^{+}\gamma_L^{-}} + \sqrt{\gamma_L^{+}\gamma_S^{-}}) \qquad \text{Eq. (10)}$$

In order to determine the surface energy components of a solid surface using **Equation 10**, contact angle measurements must be taken using at least three liquids where all the surface tension components (γ^{LW}, γ^{+}, and γ^{-}) are known. In order to ensure the solution is mathematically robust, the surface energy components of the solid are determined using the liquid/solid contact angles (θ_{eq}) and surface tension parameters of at least four liquids.

Determining the surface energy components using the van Oss-Chaudhury-Good (vOCG) model allows us to calculate the equilibrium contact angle, θ_{eq}, independently.

3.2 Methods

Solid wettability in fluid/fluid systems was examined using a vapor/water, a decane/water, and an octanol/water system. The two oils were chosen based on their polarities with respect to water. All experiments used deionized water (Barnstead Easy Pure II System, 18.2 MΩ) at pH 5 and 1 mM NaCl. Fluid properties are listed in **Table 1**.

Table 1. Relevant properties of fluids used in this study [52]

Name	Density (ρ) [g/cm^3]	Viscosity (η) [mPa s]	Dielectric constant (ε_r) at 20°C	Water interfacial tension (γ) [dyne/cm]
air	0	0	0	72.8
n-decane	0.730	0.92	1.99	51.2
1-octanol	0.822	7.288	10.3	8.5
Water	0.999	1	80.4	--

For every system, the orientation of the droplet used to measure the water contact angle was dependent on the wetting order, as shown in **Figure 3.4**. Sessile water droplets were used to determine the contact angle when water was the secondary wetting fluid and inverted sessile oil/air droplets were used when water was the primary wetting fluid. All contact angles are reported as measured through the water phase.

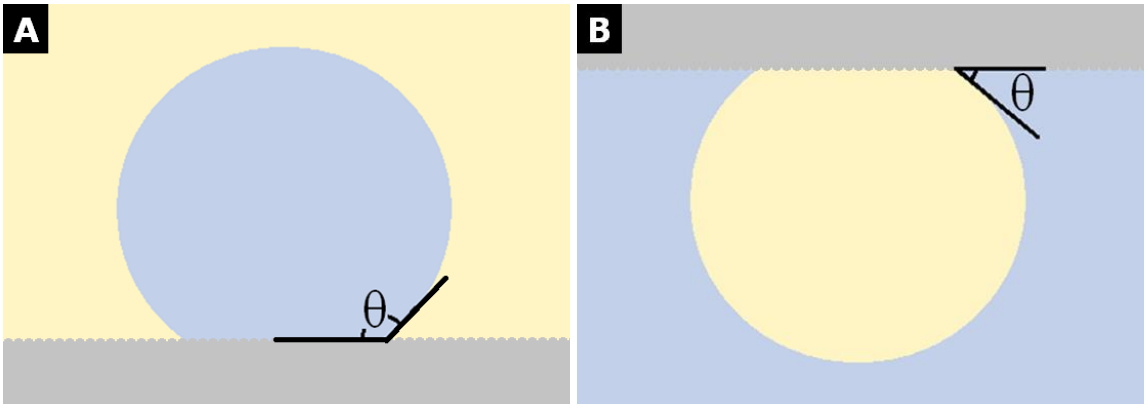

Figure 3.4. Orientation of the droplet used to measure the contact angle of a rough substrate in (A) sessile and (B) inverted sessile droplet measurements.

Contact angles were measured with a ramé-hart goniometer. Images from each experiment were processed using DropImage Advanced software to obtain the contact angle. The apparent equilibrium contact angle was determined using two different methods: the static contact angle method and the hysteresis method. The static contact angle method obtained the apparent equilibrium contact angle (θ_{stat}) directly by measuring the three phase contact angle of an axisymmetric drop that had been deposited onto the solid surface. The hysteresis method experimentally measured the advancing contact angle, θ_{adv}, and the receding contact angle, θ_{rec}. The apparent equilibrium contact angle (θ_{avg}) was calculated from the cosine average of the two measured contact angles.

3.2.1 Static contact angle method

In order to measure the static contact angle, a syringe deposited an axisymmetric, 2 μL droplet onto the solid surface. The droplet volume was small enough that gravitational effects could be neglected [53]. The goniometer software reported the droplet contact angle every 0.2 s. An equilibrium state was assumed when there was no visible change in the droplet width or the reported contact angle. For the water/vapor and water/decane system, this typically took between 10 s and 60 s. Droplet spreading for the octanol/water system usually took between 1 and 5 min.

The static contact angle method assumes that the as-placed droplet will eventually reach an equilibrium state [15]. This is a problematic assumption, particularly for physically heterogeneous surfaces where surface features can pin the droplet contact line, trapping the droplet in a non-equilibrium state [15, 54, 55]. A more effective method of determining the apparent equilibrium contact angle relies on the average contact angle. Experimentally, slow movement of the contact line caused by growing or retracting a droplet forces the drop out of non-equilibrium states, preventing any effect of contact line pinning [54].

3.2.2 Hysteresis method

The hysteresis method determines the apparent equilibrium angle either by averaging the advancing and receding contact angles [56]:

$$\theta_{avg} = \frac{\theta_{adv} + \theta_{rec}}{2} \qquad \text{Eq. (11)}$$

or by averaging the cosine of the advancing and receding contact angles [57]:

$$\cos(\theta_{avg}) = \frac{\cos(\theta_{adv}) + \cos(\theta_{rec})}{2} \qquad \text{Eq. (12)}$$

Both averaging procedures assume that θ_{adv} and θ_{rec} are equidistant from the apparent equilibrium contact angle, θ_{avg}. Despite this extremely simplifying assumption, θ_{avg} is very similar to the equilibrium contact angle predicted using the Young equation for smooth surfaces [56-59]. Unlike the static contact angle method, the droplet size is not limited in the hysteresis method and can be as large as 100 μL, as long as the droplet remains axisymmetric [53].

In this study, droplets were grown and retracted in order to experimentally observe θ_{adv} and θ_{rec}. The difference between θ_{avg} determined using **Equation 11** and **Equation 12** was insignificant. An example is shown in **Figure 3.5**.

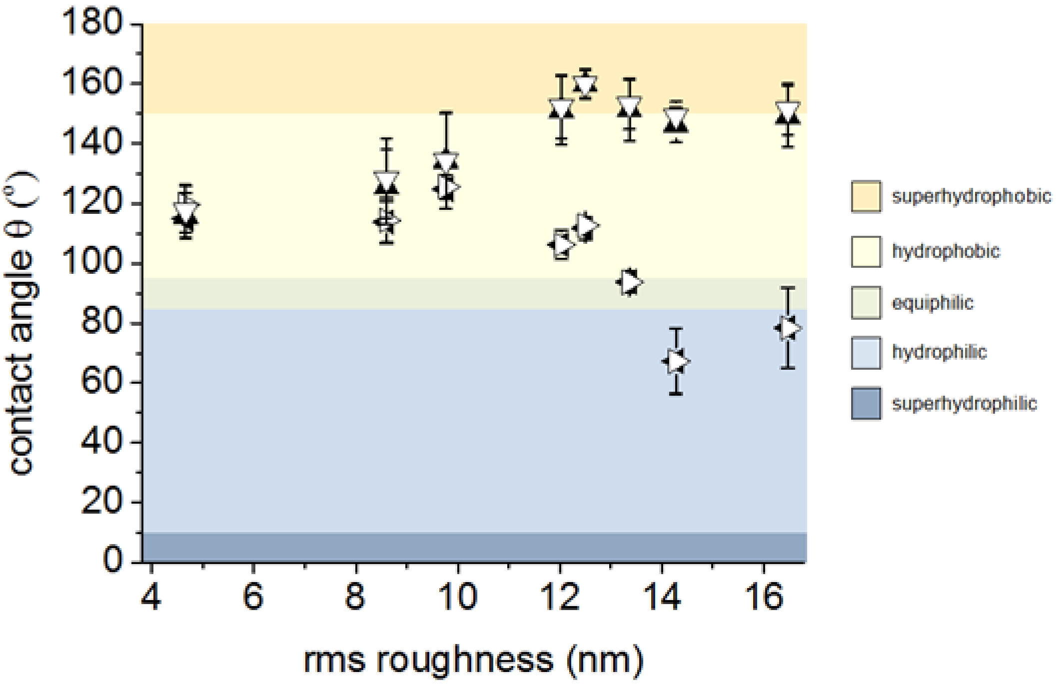

Figure 3.5. Comparison of θ_{avg} determined using Equation 11 (open symbols) and Equation 12 (closed symbols) for sessile water droplets in octanol (▽,▲) and inverted sessile octanol droplets in water (▷,◀).

Advancing and receding contact angles were obtained by slowly growing or retracting an axisymmetric droplet with a syringe pump (New Era Pump Systems Inc., NE-300). Droplets were grown or retracted at a constant rate of 0.1 µL/s to suppress any dynamic effects on θ_{adv} or θ_{rec} [53]. The process is shown below in **Figure 3.6** for a sessile water droplet, but the same method was used for inverted sessile droplets.

A droplet of the wetting liquid was first deposited onto the solid surface (**Figure 3.6.A**). The droplet was then slowly grown by increasing the droplet volume. The droplet contact angle increased until it reached θ_{adv} (**Figure 3.6.B**), at which point the droplet baseline began to increase, shown in **Figure 3.6.C**. θ_{adv} remained constant the entire time the droplet was grown.

In order to measure the receding contact angle, droplet fluid was slowly removed through the syringe needle. The droplet contact angle decreased until it reached θ_{rec} (**Figure 3.6.D**), at which point the droplet baseline began to decrease (**Figure 3.6.E**). When the droplet width approaches the dimension of the needle diameter, the droplet shape began to distort and the contact angle decreased rapidly to zero (**Figure 3.6.F**).

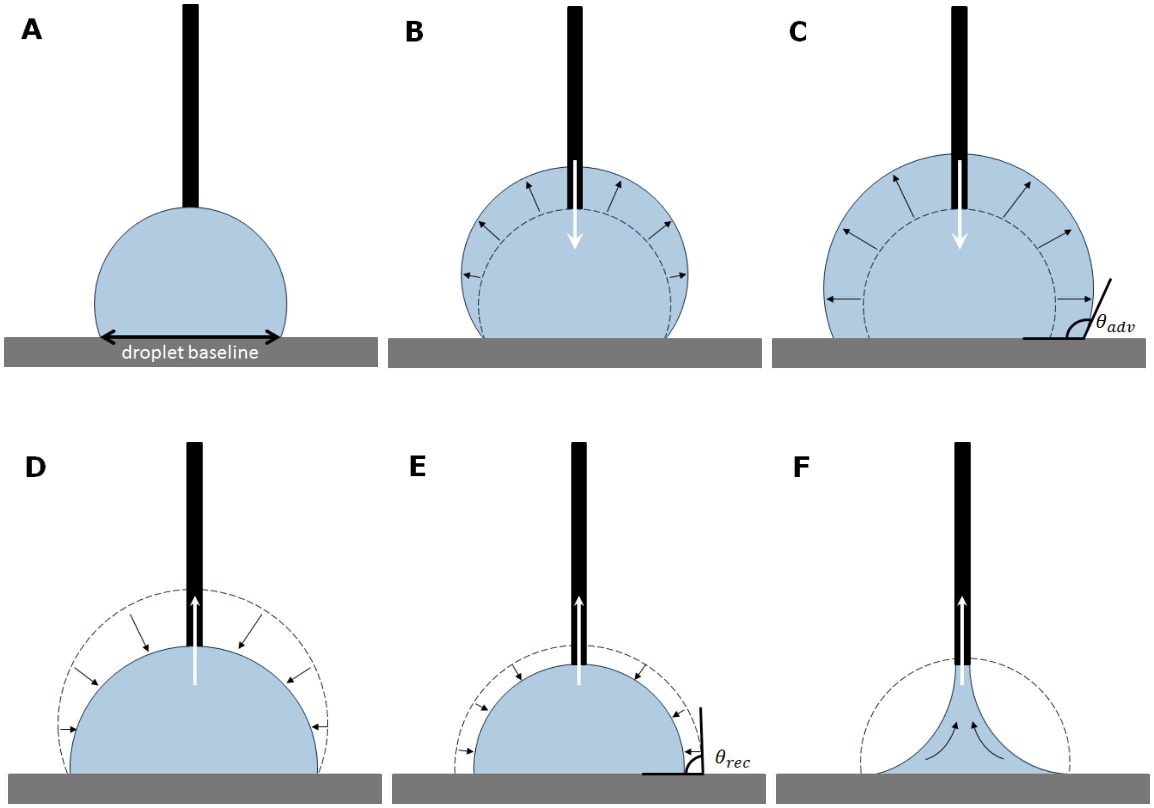

Figure 3.6. Scheme depicting the different stages of droplet growth to determine θ_{adv} (A-C) and retraction to determine θ_{rec} (D-F). (A) A droplet of the wetting liquid is initially deposited onto the surface. (B) Liquid is slowly pumped into the droplet and the contact angle increases. (C) Once the contact angle reaches θ_{adv}, the droplet baseline width begins to increase while θ_{adv} remains constant. (D) When liquid is initially retracted from the droplet, the liquid contact angle decreases but the three phase contact line does not change. (E) When the droplet contact angle reaches θ_{rec}, the droplet baseline width begins to decrease. (F) Once the volume of the droplet is the same magnitude as the size of the needle, the droplet shape begins to distort and the observed contact angle is no longer meaningful for determining θ_{avg}.

Experimentally, the receding contact angle is much more difficult to obtain than the advancing contact angle. In the ideal case, the receding contact angle remains constant during the entire time the droplet is retracted. An example is shown in **Figure 3.7.A**. θ_{rec} is then the average of all the measured θ_{rec} values. In non-ideal cases, the receding contact angle can follow one of three different patterns: (1) θ_{rec} decreases with time (2) θ_{rec} follows a “stick/slip” pattern (3) no θ_{rec} is observed [60]. An example of the first pattern is shown in **Figure 3.7.B**.

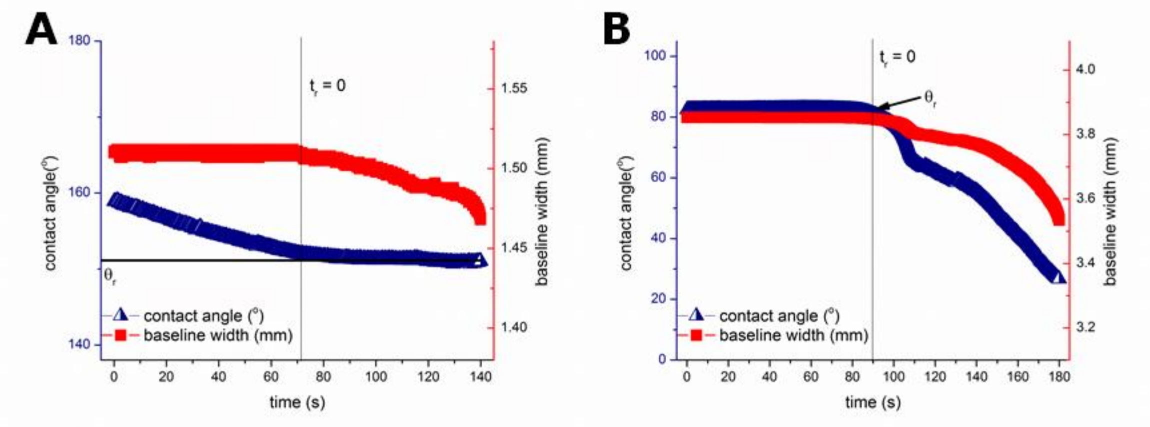

Figure 3.7. (A) Constant θ_{rec}: once the receding contact angle is reached, the droplet width begins to decrease without changing the droplet contact angle. (B) Time-dependent θ_{rec}: the measured receding contact angle decreases with the droplet baseline.

In this study, only the ideal case and the first pattern were observed. In the non-ideal case, the calculated θ_{rec} was defined as the contact angle observed just as the drop baseline began to decrease.

3.2.3 Measurement of surface energy components

In order to determine the surface energy of the solid surface, the three surface tension components, γ^{LW}, γ^{+}, and γ^{-}, were calculated using the vOCG model (**Equation 10**). In principle, measuring 3 solid/liquid contact angles using reference liquids with known surface tension components recover the unknown surface tension components (γ^{LW}, γ^{+}, and γ) of the solid surface. The method becomes much less sensitive to experimental error when 3 unknowns are fit to 4 equations [61].

Similarly, the surface tension components for each liquid used in this study could have been determined using **Equation 7** by measuring 4 interfacial tensions with an immiscible reference liquid with known surface tension parameters. Literature values for the liquids used in this study were already available, so determining the surface tension experimentally was unnecessary. Liquid properties are listed in **Table 2**.

Table 2. Surface tension components and parameters for relevant liquids at 20°C, in mJ/m^2 [46]

liquid	γ^{LW}	γ^{AB}	γ^{+}	γ^{-}	γ
water	21.8	51	25.5	25.5	72.8
glycerol	34	30	3.92	57.4	64
diiodomethane	50.8	0	0	0	50.8
dimethylsulfoxide	36	8	0.5	32	44
1-octanol	27.5	0	0	18	27.5
n-decane	23.83	0	0	0	23.83

Contact angle measurements were made using sessile ethylene glycol, diiodomethane, glycerol, and water droplets on the smoothest available polymer surfaces (substrates treated with 60% acetone).

The calculated surface energy components for the polymer substrate will not be an exact representation of the surface energy, since measured contact angle measurements were treated as Young equilibrium contact angles (θ_{eq}) and SEM images clearly show that the substrates used for the contact angle measurements had a residual degree of surface roughness. They may nonetheless serve as a useful approximation.

Solid surface tension components were determined using **Equation 10** and are listed in **Table 3**. Each contact angle was the average of at least four measurements.

Table 3. Calculated surface tension components for ES-100 polymer substrates at 20°C, in mJ/m^2

γ^{LW}	γ^{+}	γ^{-}	γ
38.73 ± 0.84	0.62 ± 0.03	20.98 ± 1.61	45.92 ± 0.94

Most polar polymer surfaces have a $\gamma^{LW} \approx 40$ mJ/m^2 ± 10% and are usually electron donors. Considering that ES-100 is a co-polymer of PMMA and PMAA, which both have a surface energy of ~41 mJ/m^2, it makes sense that the surface appears polar [62, 63]. The calculated surface energy is slightly higher than expected, but is within error.

The liquid/solid interfacial tensions for a sessile liquid droplet in air were calculated using the known surface tension components (**Table 4**).

Table 4. Liquid/solid interfacial tensions at 20°C, in mJ/m^2

Liquid	γ_{LS}
n-decane	8.98 ± 0.28
water	6.42 ± 1.27
1-octanol	1.27 ± 0.40

In general, the solid/liquid interfacial tensions appear quite low, and γ is especially low for octanol, which suggests a very high surface affinity for octanol. After the surface tension components for the polymer surface were determined, equilibrium contact angles for the fluids used in this study were calculated using the Young equation (**Table 5**).

Table 5. Comparison of calculated and experimentally measured equilibrium contact angles for smoothest polymer surfaces

Non-aqueous phase	θ_{eq} for the smoothest surface		
	calculated	Sessile water in oil/air	Inverted sessile oil/air in water
air	57.15 ± 2.07	48.43 ± 10.24	54.00 ± 4.48
n-decane	87.29 ± 1.64	76.34 ± 4.63	94.34 ± 3.38
1-octanol	128.68 ± 15.54	115.92 ± 7.69	115.05 ± 4.81

The theoretical predictions for the contact angle clearly reflect the same trends as the experimental contact angles. There is nonetheless a noticeable difference between the calculated and measured equilibrium contact angles (θ_{eq}) for all three systems. The difference is not entirely surprising since the vOCG model is still somewhat controversial. It is, however, the only model that allows for the characterization of acid-base components of solids and liquids within the same framework. In addition to the assumptions used to determine the surface tension components of the polymer substrates, $\theta_{eq,expt}$ were measured using 60% treated substrates, which are not completely smooth.

3.2.4 Modeling surface wettability

Once the equilibrium contact angle for the ideal surface was calculated, the effect of surface roughness solid wettability was described using a model that contained a Wenzel wetting regime and a Cassie-Baxter wetting theories, which we called the Wenzel/Cassie-Baxter model. Based on SEM images of the roughest substrates (**Figure 2.4**), each unit cell of the substrate was modeled as a spherical particle of radius R_s on a square with the area $(2R_s)^2$ (**Figure 3.8.A**). To simulate the change in roughness observed in the SEM images, the spherical particle was "pushed" further into the surface. Substrates treated with 60% acetone solutions were represented with a spherical cap with a height of 0.1 R_s (**Figure 3.8.B**).

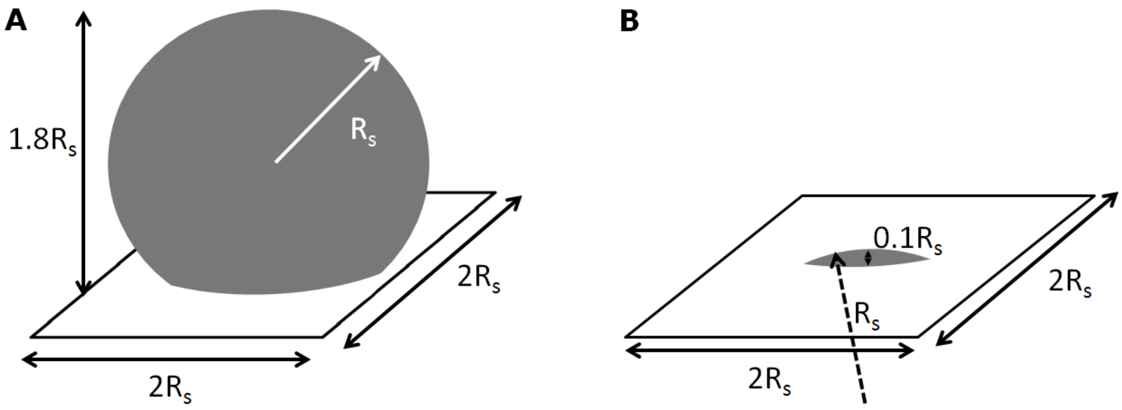

Figure 3.8. Unit cell for wetting model for (A) the roughest and (B) smoothest substrate

The Wenzel model assumes that the entire substrate is wetted by the droplet fluid. In this study, the Wenzel model was only valid for substrates with minimal to moderate roughness in the water/vapor and water/octanol system (substrates treated with 35% - 60% acetone solution). For very rough substrates, $\cos^{-1}(r_W \cos(\theta_{eq}))$ was not a real number.

The Cassie-Baxter model divides the wetted area into two parts: the area of the droplet in contact with the solid surface, f_1, and the area of the droplet in contact with the primary wetting fluid, f_2. Traditionally, the Cassie-Baxter theory assumes that the asperities are perfectly smooth and the surrounding fluid completely fills the interstitial spaces between roughness features (**Figure 3.9**). A modified set-up was used to describe the system in the Cassie-Baxter wetting regime, shown in **Figure 3.10**.

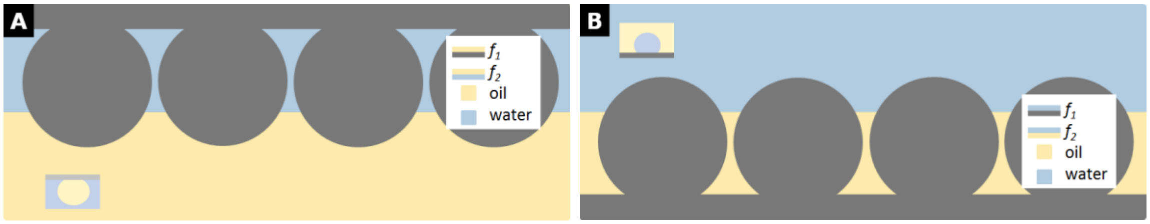

Figure 3.9. Traditional representation of a rough substrate in Cassie-Baxter wetting regime for (A) an inverted oil droplet in water and (B) a sessile water droplet in oil. The macroscopic image of the droplet for each scenario is shown in the inset.

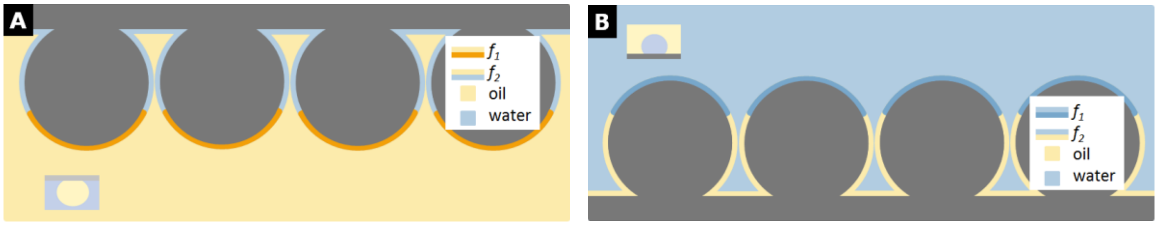

Figure 3.10. Representation of rough substrate in Cassie-Baxter wetting regime in this study's model for (A) an inverted oil droplet in water and (B) a sessile water droplet in oil. The macroscopic image of the droplet for each scenario is shown in the inset.

In this study, we assumed that the density difference between the droplet fluid and the primary wetting fluid caused the droplet to push out most of the fluid in the interstitial space between the rough features ("overhanging parts" or "re-entrant features"). The primary wetting fluid would not be completely removed and result in a state where a thin film of the primary wetting fluid surrounded part of the roughness features to simulate the entrapment of the primary wetting fluid in the roughness features of the polymer particles. This method to describe $f_1$and f_2 has been employed for super-hydrophobic surfaces with hierarchical roughness structures [64, 65] and is supported by recent evidence of intermediate wetting states characterized by a combination of Wenzel and Cassie-Baxter wetting [66]. The consequence of using this particular set-up was the decreased ratio of f_1 to f_2 compared to the traditional model.

Despite the disparity between calculated and measured equilibrium contact angles (**Table 5**), using $\theta_{eq,calc}$ as the Young equilibrium contact angle when fitting wetting behavior for all three fluid/fluid systems adequately described the observed wetting behavior, which will be further discussed in the following section.

3.3 Results

Without considering the effects of surface roughness, the order of wetting and the choice of reference fluids already have a significant effect on solid surface wettability. As shown in **Table 6**, the choice of reference fluids changes the apparent hydrophobicity of smooth substrates. The hydrophobicity of the smoothest substrate (treated with 60% acetone solution) increases with the relative polarity of the non-aqueous fluid.

Table 6. Apparent equilibrium contact angle determined using cosine average of θ_{adv} and θ_{rec}

Non-aqueous phase	Sessile water droplet	Inverted sessile droplet in water
Air	48.42 ± 10.25	55.68 ± 3.51
n-decane	76.34 ± 4.63	94.34 ± 3.38
1-octanol	115.92 ± 7.69	115.05 ± 4.81

In this study, the droplet contact angle determined using the hysteresis method was usually smaller than the contact angle determined using the static contact angle method. Of the two methods, the contact angle determined using the averaging procedure is a better representation of the actual surface wettability. In the static contact angle method, the droplet spreads on the surface with a contact angle $\theta_{eq} < \theta < \theta_{adv}$. If the contact line becomes anchored on a surface defect, the measured contact angle will be larger than the equilibrium contact angle. Forcing the three phase contact line to move by growing and shrinking the droplet minimizes the effect of contact line pinning, resulting in a more accurate measurement of the apparent equilibrium contact angle.

3.3.1 Vapor/water systems

Contact angle measurements from this study indicate that the effect of surface roughness on surface wettability of ES-100 polymer substrates is strongly affected by the wetting order (**Figure 3.11**).

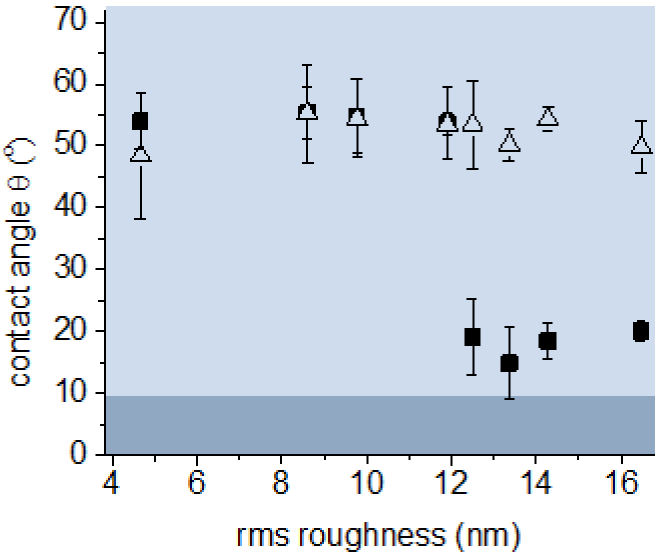

Figure 3.11. Average contact angle measurements in a water/air/ES-100 system for sessile water droplets in air (Δ) and inverted sessile air bubbles in water (■)

The contact angle for a sessile water droplet in air remains constant despite changing surface roughness, but a significant roughness-dependent change in surface wettability is observed when water is the primary wetting liquid. Curiously, the change in surface wettability takes the form of a step change when the rms roughness is approximately 12 nm, which corresponds to surfaces treated with 35% acetone solutions and suggests that the change in wetting behavior is based on the shape of the surface roughness rather than the amplitude. SEM images show that surfaces treated with acetone solutions with 10% - 30% acetone solutions are coated with discrete particles with many overhanging parts. The gaps between the particles begin to disappear when the surfaces are treated with 30% to 40% acetone solutions, after which the substrates have more of a wavy roughness.

The relatively constant contact angle can be explained as the result of a transition from Wenzel to Cassie-Baxter wetting (**Figure 3.12.A**). When an inverted sessile air droplet is placed in water, a step change in the apparent equilibrium contact angle is observed that is consistent with a wetting transition (**Figure 3.12.B**).

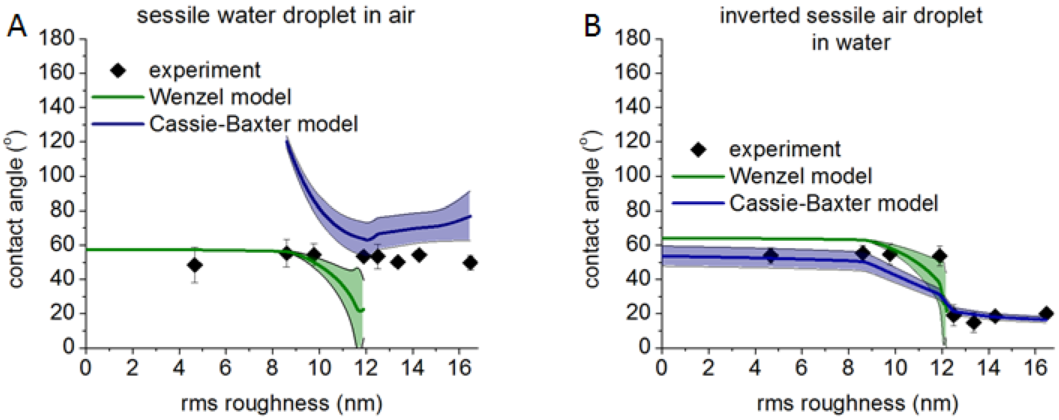

Figure 3.12. The Wenzel and Cassie-Baxter models can be used to describe the observed wetting behavior for (A) sessile water droplets in air and (B) inverted sessile air droplets in water. The 95% confidence interval (two standard errors of the mean) is shown by the shaded area.

For the water/air system, the Wenzel model could not be plotted for the entire range because for very rough substrates, there was no solution to **Equation 3**. The 95% confidence interval was calculated using a Gaussian distribution around the sample mean.

The Cassie-Baxter model drastically over-predicts the apparent contact angle for sessile water droplets on rough substrates (**Figure 3.12.A)**. This error is minimized by accounting for the large density difference between air and water (**Figure 3.13**). The model used in this study assumes that for each asperity, most of the surface is covered with a thin film of the primary wetting fluid. Due to the large density difference between water and air, a more likely configuration assumes that the water droplet pushes out most of the air trapped in the interstitial spaces and only a small percentage of the total wetted area consists of an air/water interface. If we assume the water/solid contact area (f_1) makes up 95% of the total wetted area, the Cassie-Baxter model better explains wetting behavior for rough surfaces.

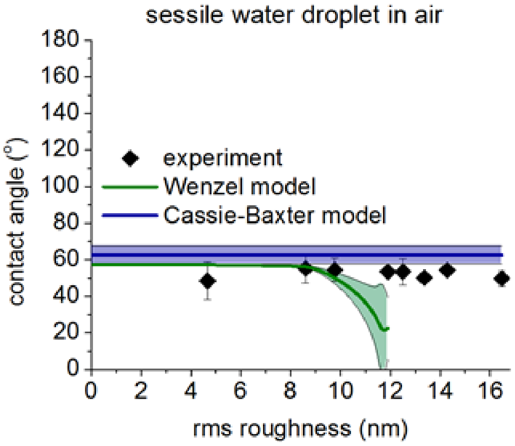

Figure 3.13. A modified model when the water is assumed to wet 95% of the total contact area (f_1 + f_2) better describes the observed wetting behavior for a sessile water droplet in air. The 95% confidence interval (two standard errors) is shown by the shaded area.

The model still over-predicts the observed contact angle because the equilibrium contact angle determined using the Young equation (**Table 3.6**) is larger than the observed contact angle for the smoothest substrates (**Table 3.5**).

With this modification to the Cassie-Baxter model, it is no longer clear if a roughness-dependent wetting transition exists for sessile water droplets in air.

3.3.2 Oil/water systems

In the decane/water system, the substrates are no longer unambiguously hydrophilic (**Figure 3.14)**. The smoothest surfaces appear “equiphilic”, with an apparent equilibrium contact angle around 90^o, most likely because liquid/solid interfacial tensions for ES-100/decane and ES-100/water are very similar (**Table 4**).

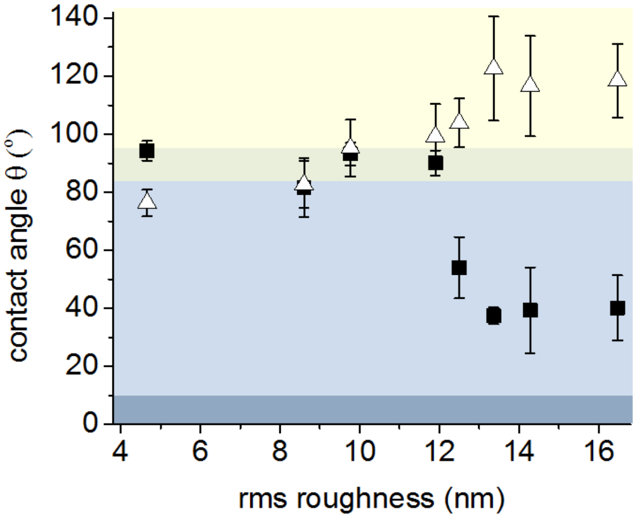

Figure 3.14. Average static contact angle measurements in a water/decane/ES-100 system for sessile water droplets in air (Δ) and inverted sessile air bubbles in water (■)

From the contact angle measurements, it is clear that regardless of wetting order, rough substrates in the decane/water system exhibit Cassie-Baxter wetting behavior: surfaces become increasingly hydrophobic with increasing surface roughness when decane is the primary wetting liquid and hydrophilic when water is the primary wetting liquid. It is unclear if a wetting transition exists when water is the secondary wetting liquid (**Figure 3.15.A**), since both Wenzel and Cassie-Baxter models predict similar behavior for smooth surfaces. When water is the primary wetting liquid, the Cassie-Baxter model better describes wetting behavior for rough surfaces (**Figure 3.15.B**).

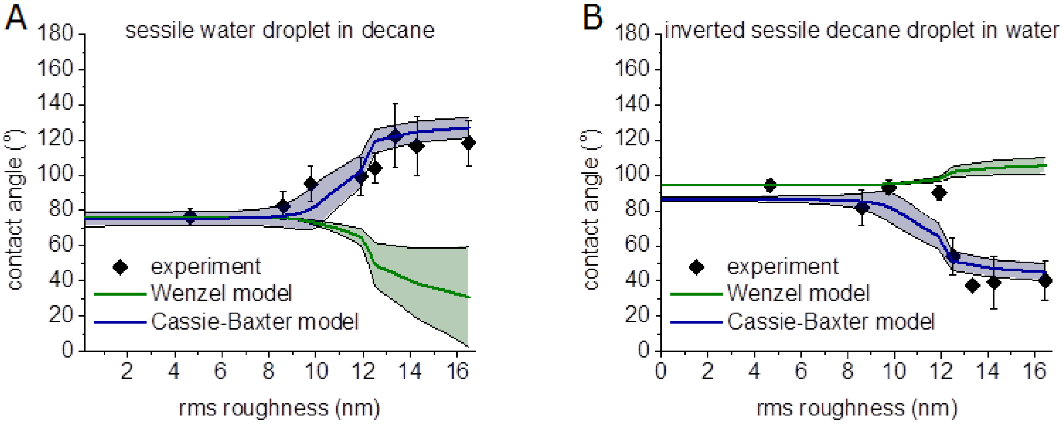

Figure 3.15. The Wenzel and Cassie-Baxter models can be used to describe the observed wetting behavior for (A) sessile water droplets in decane and (B) inverted sessile decane droplets in water. The 95% confidence interval (two standard errors) is shown by the shaded area.

As shown in **Figure 3.16**, the smoothest surfaces appear unambiguously hydrophobic ($\theta_{app,eq} > 90^o$) in an octanol/water system, regardless of wetting order. The octanol/ES-100 interfacial tension is also about four times lower than the water/ES-100 interfacial tension (**Table 3**). Thus, smooth ES-100 polymer surfaces have a much higher affinity for octanol than water.

The octanol/water system is the only one in this study that exhibits order-dependent wetting behavior and shows the strongest evidence of a wetting transition from the Wenzel to Cassie-Baxter regime. When octanol is the primary wetting liquid, increasing the surface roughness increases the apparent hydrophobicity of the substrate, which is consistent with either Wenzel or Cassie-Baxter wetting. When water is the primary wetting liquid, a change in surface roughness appears to first increase the surface hydrophobicity, consistent only with Wenzel wetting. However, the fact that the roughest surface appears hydrophilic strongly suggests Cassie-Baxter wetting of these surfaces.

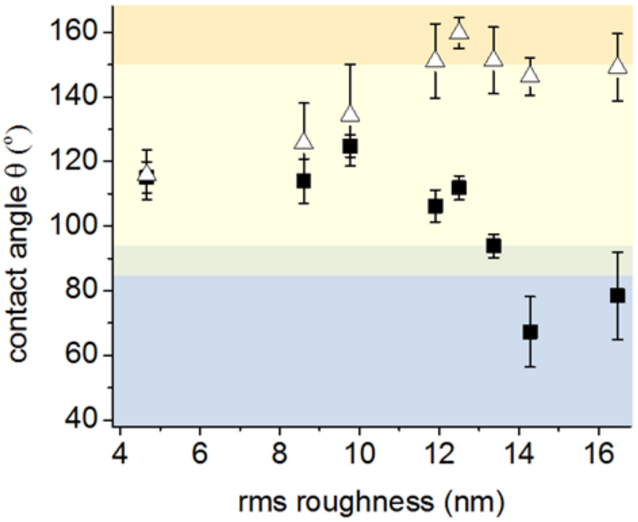

Figure 3.16. Average contact angle measurements in a water/octanol/ES-100 system for sessile water droplets in octanol (Δ) and inverted sessile decane droplets in water (■)

The hypothesized order-dependent wetting regimes are further supported by the Wenzel/Cassie-Baxter model (**Figure 3.17**). When octanol is the primary wetting liquid, it is unclear if a transition from Wenzel to Cassie-Baxter occurs with increasing surface roughness, as both theories describe roughness-dependent wetting for substrates of smooth to moderate roughness (**Figure 3.17.A**). Only when water is the primary wetting liquid do we see the evidence supporting a roughness-dependent wetting transition (**Figure 3.17.B**).

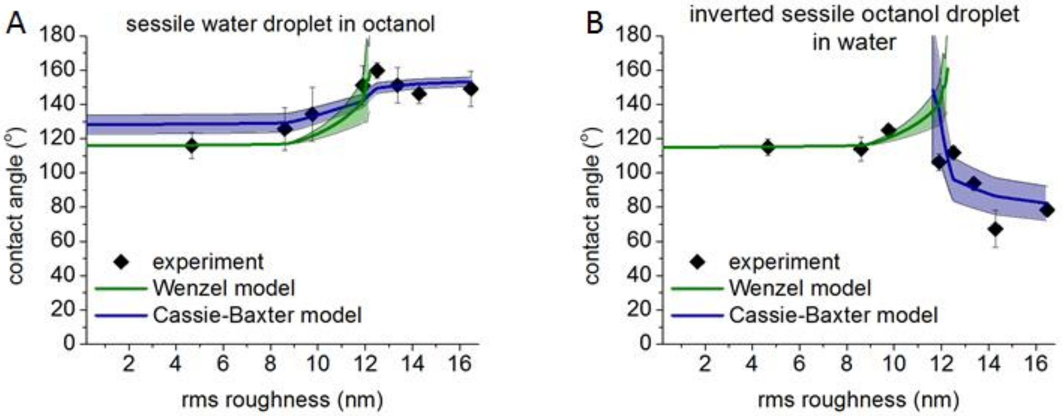

Figure 3.17. The Wenzel and Cassie-Baxter models can be used to describe the observed wetting behavior for (A) sessile water droplets in octanol and (B) inverted sessile octanol droplets in water. The 95% confidence interval (two standard errors) is shown by the shaded area.

The Cassie-Baxter theory cannot be used to describe the wetting behavior of smooth substrates in an octanol/water system with water as the primary wetting liquid for substrates when the rms roughness ≤ 10 nm ($f_2 < 0$). Wetting behavior of smoother substrates and the slight increase of the observed contact angle as the surface roughness increases to moderate roughness is only consistent with the Wenzel theory.

3.4 Concluding remarks

The combined effects of surface roughness, wetting order, and choice of reference fluids on equilibrium wetting behavior were examined. Surface wettability in each system was quantified using contact angle measurements and solid surface energy components were determined using the vOCG model. The effect of surface roughness on the observed wetting behavior was categorized using either the Wenzel or Cassie-Baxter theory.

Regardless of surface roughness, surface hydrophobicity increased with the polarity of the non-aqueous fluid. Substrates appeared the hydrophobic in the octanol/water system, equiphilic in the decane/water system, and hydrophilic in the water/air system. Apparent hydrophobicity was determined using contact angle measurements and the dependence of surface wettability on fluid polarity corresponded to liquid/solid interfacial tensions determined using the vOCG model.

The roughest substrates in every tested system exhibited Cassie-Baxter wetting behavior. The Wenzel model could only describe wetting behavior for substrates with little to moderate roughness (corresponding to substrates treated with 30% acetone or less). For every system where a liquid was the primary wetting fluid, the Cassie-Baxter theory adequately described roughness dependent wetting behavior with the exception of the octanol/water system. Since none of the surfaces tested were atomically smooth, it is possible that some of the primary wetting fluid remained trapped in surface defects of the smoothest surfaces, resulting in contact angle measurements that could be described using Cassie-Baxter wetting assumptions. The small degree of surface roughness for the smoothest substrates used to determine θ_{eq}, shortcomings in the vOCG model, and error in literature values for the reference liquids all accounted for the discrepancy between θ_{eq} determined using the Young equation and the experimentally determined θ_{eq}. Despite the discrepancy for the equilibrium contact angles, the Wenzel/Cassie-Baxter model adequately describes roughness-dependent wetting behavior.

The octanol/water system with water as the primary wetting liquid provided the strongest evidence of a roughness-dependent wetting transition from Wenzel to Cassie Baxter wetting. The transition point corresponded to a change in the shape of surface roughness features, from wavy roughness to particles with discrete particles. The octanol/water system also provided the clearest example of order-dependent wetting behavior: increasing surface roughness resulted in a transition from hydrophobic to hydrophilic behavior only when water was the primary wetting liquid [67, 68].

Wetting behavior in liquid/liquid systems is complex and dependent on many different factors. In particular, effects of increasing surface roughness are system dependent but the roughest substrates exhibit Cassie-Baxter wetting, most likely due to the gaps between the particles.

This part of the study focused on equilibrium wetting behavior of one particular polymer surface, ES-100. Future studies using other polymer surfaces will determine the universality of the observed wetting behavior or if the roughness and wetting fluid trends in this study are specific to the systems studied here.

A definitive wetting transition from Wenzel to Cassie-Baxter wetting was observed only for the octanol/water system. This study concluded that the relative polarity of the oil phase determined whether or not a wetting transition occurred; future studies using an oil with an intermediate dielectric constant, such as diiodomethane (ε_r = 5.32 at 25^{o}C), are expected to yield further insights into the connection between oil polarity and roughness-induced wetting transitions.

CHAPTER 4

DYNAMIC WETTING BEHAVIOR

4.1 Background

Spreading kinetics a liquid droplet with radius *R* can be described by relating the change in the width of the wetted area, *r*, or the dynamic contact angle, θ_d, to time (**Figure 4.1**). In the past hundred years, two theories have been used to describe the spreading of a liquid droplet on a solid surface. The hydrodynamic theory (HDT) describes droplet spreading in terms of macroscopic fluid flow while the molecular kinetic theory (MKT) describes droplet spreading as the result of liquid/solid molecular interactions.

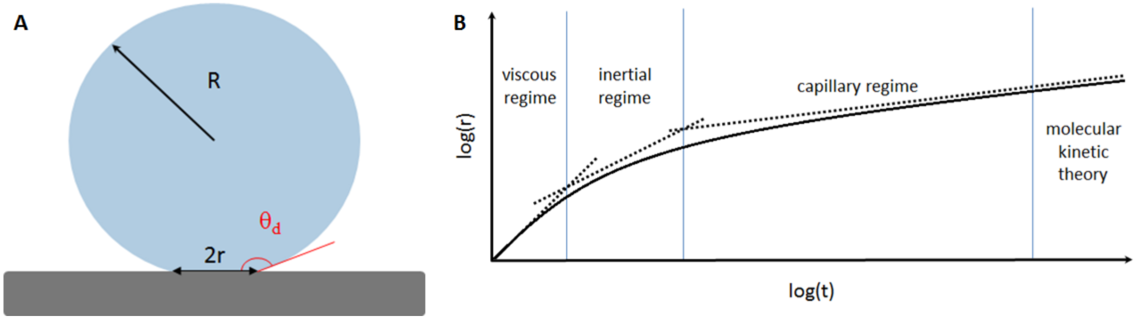

Figure 4.1. (A) A schematic of the relevant length scales for a spreading droplet and (B) the sequence of spreading regimes associated with the hydrodynamic and molecular kinetic theories of droplet spreading.

In order for early droplet spreading to be described using the HDT or MKT, gravitational effects must be negligible compared to surface tension forces. The Bond number (Bo), a dimensionless number that describes the ratio of the two forces, must be less than 1:

$$\mathrm{Bo} = \frac{\Delta\rho g L^2}{\gamma} \qquad \text{Eq. (13)}$$

where $\Delta\rho$ is the density difference between the droplet and surrounding fluid, g is the gravitational force, L is the characteristic length (the radius of the droplet, R), and γ is the interfacial tension between the droplet and surrounding fluid.

When the droplet is near equilibrium, molecular interactions between the liquid and solid dominate the movement of the contact line and droplet spreading can be described using MKT. The capillary number (Ca), a dimensionless number that represents the relative contributions of viscous forces and surface tension forces, is used to determine when MKT is applicable:

$$\mathrm{Ca} = \frac{\eta v}{\gamma} \qquad \text{Eq. (14)}$$

where η is the liquid viscosity, v is the velocity of the moving contact line, and γ is the interfacial tension. In order for molecular interactions to be the dominant driving force for droplet spreading, Ca must be less than 10^{-4}, an empirically determined threshold [1, 19]. For the systems studied here, Ca was always larger than 10^{-4} for the duration of the experiment.

4.1.1 The hydrodynamic theory

When a liquid droplet comes into contact with a solid, surface tension forces drive the droplet to spread until it reaches its equilibrium state. The hydrodynamic theory describes spreading behavior from the moment of contact to minutes afterward. The theory can be further broken down into three main regimes: the viscous regime, the inertial regime, and the capillary regime. The viscous and inertial regimes are defined by the predominant force opposing surface tension [21]. In the capillary regime, the dominant force opposing surface tension is also the viscous force, but was named the capillary regime to avoid confusion. The transitions between each regime are determined by comparing the relative magnitudes of forces resisting surface tension.

The examination of the viscous and inertial regimes has mostly been done in liquid/vapor systems, while the equations governing spreading behavior in the capillary regime have been applied to liquid/vapor and liquid/liquid systems. Surface properties only begin to affect observed spreading behavior in the capillary regime [17, 20, 22, 24, 69, 70].

In the viscous and inertial regimes, the curvature of the droplet, defined using the radius of curvature, r_{gap}, is extremely high near the contact point (**Figure 4.2.A**). The high curvature generates rapid fluid flow within the droplet, which drives spreading. Since $r_{gap} \ll R$, a droplet spreading on a solid surface is analogous to the coalescence of two drops (**Figure 4.2.B**).

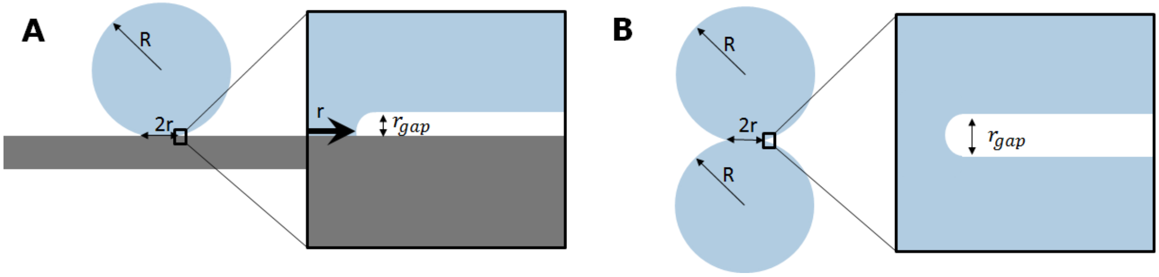

Figure 4.2. The spreading of a liquid droplet on (A) a solid surface can be approximated as (B) the coalescence of two liquid droplets of equal radius.

In the initial stages of drop coalescence, the surface of the droplets can be described using geometric arguments (**Figure 4.3**).

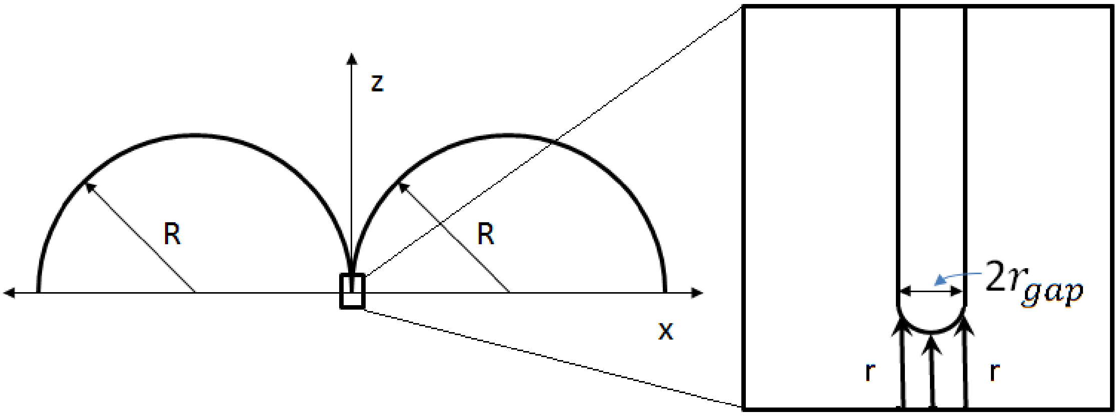

Figure 4.3. The characteristic length, r_{gap}, can be related to macroscopic lengths, *r* and *R*, using geometric arguments

For the touching hemispheres (with x and z as the horizontal and vertical axis in **Figure 4.3**):

$$\boldsymbol{R^2 = z^2 + (R - x)^2 \approx z^2 + R^2 - 2Rx} \qquad \text{Eq. (15)}$$

for $x \ll R$, from which **Equation 16** follows when *x* is identified as the gap half-width r_{gap} and *z* as the wetting radius *r*. The characteristic length, r_{gap}, can be related to macroscopic quantities, *r* and *R*, via:

$$\boldsymbol{\frac{r}{R} = (\frac{2r_{gap}}{R})^{1/2}} \qquad \text{Eq. (16)}$$

when z > 0. The relevant radius of curvature, the width of the gap, is therefore:

$$r_{gap} = \frac{r^2}{2R} \qquad \text{Eq. (17)}$$

Very close to the contact point ($r \ll 1$), the "walls" of the gap are nearly parallel and surface tension forces only act on the meniscus with curvature $\kappa = 1/r_{gap}$.

4.1.2 Viscous spreading regime

In the instant of liquid/solid contact, surface tension forces force the droplet to spread while being opposed by liquid viscous forces. Exact mathematical solutions describing early spreading behavior in the viscous regime show that the radius of the wetted area, r_{visc}, scales linearly with time [24, 71, 72]:

$$r_{visc} \sim \frac{\gamma\tau}{\eta} \qquad \text{Eq. (18)}$$

where γ is the interfacial tension, η is the drop viscosity, and $\tau = t - t_0$, which accounts for the experimental uncertainty in the time measurement. In this study, $t_0 = 0$. As seen from **Equation 18**, spreading in the viscous regime is independent of surface wettability. The length of the viscous regime is determined using the Reynolds number, which relates the viscous and inertial forces:

$$\text{Re} = \frac{\rho v r_{gap}}{\eta} \qquad \text{Eq. (19)}$$

where ρ is the drop density, v is the velocity of the contact line, and η is the drop viscosity. The crossover between the viscous and inertial regime occurs when Re = 1.

4.1.3 Inertial spreading regime

In the inertial regime, surface tension forces are opposed by inertial forces, $F = d(mv)/dt$. Using scaling arguments, one obtains the radius of the wetted area, r_{in}:

$$r_{in} \sim (\frac{\gamma R}{\rho})^{1/4}\tau^{1/2} \qquad \text{Eq. (20)}$$

The duration of the inertial regime is largely dependent on the droplet approach velocity, radius, and liquid viscosity, but is independent of surface roughness [22, 23]. Unlike the transition between the viscous and inertial regimes, the crossover between the inertial and capillary regimes is system dependent and has usually been determined empirically [22, 70, 73]. The inertial regime lasts on the order of a few milliseconds before transitioning into the capillary regime.

4.1.4 Capillary spreading regime

In the capillary regime, spreading is driven by capillary forces. The spreading droplet is described using the spherical cap approximation (**Figure 4.4.A**). In the case of a perfectly wetting solid, θ_d is so small (≈ 0^o) that the droplet can be approximated as a wedge with height h^* and length r near the contact line (**Figure 4.4.B**) [74-76]. The capillary force (F_c) per unit length of the contact line (l) in the capillary regime is described using the Young equation (**Equation 2**) with the small angle approximation [74-77]:

$$\frac{F_c}{l} \sim \gamma \theta_d^2 \qquad \text{Eq. (21)}$$

Capillary forces are predominantly opposed by the viscous force, which characterized the losses due to viscous dissipation in the droplet. The viscous losses are determined using fluid dynamics.

Fluid dynamics usually assumes a no-slip boundary condition is usually assumed at the interface of the moving liquid and the solid surface. However, such a boundary condition would require an infinitely large force to move the three phase contact line [78]. The obvious discrepancy between theoretical predictions and experimental observations regarding contact line motion is rectified by only using the hydrodynamic theory to describe spreading behavior of the liquid at least 10 nm from the surface in the capillary regime, thereby assuming a full-slip boundary condition at the “liquid/solid” interface [1, 75, 76, 79, 80].

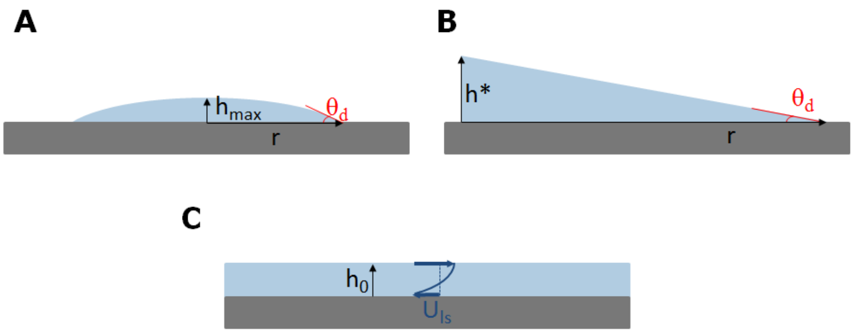

Figure 4.4. (A) In the capillary regime, the spreading droplet is described using the spherical cap approximation. (B) In the case of a perfectly wetting solid, the droplet edge is approximated as a wedge with height h^* and length *r*. (C) The lubrication approximation applied to the liquid wedge, where the velocity at the fluid velocity at the liquid/solid interface is $-U_{ls}$ and $v = v_{max}$ at $h = h_0$.

In a vapor/liquid system with a very small θ_d, the velocity profile, $v(h)$, and viscous dissipation, ξ, can be described using the lubrication approximation, which assumes the liquid wedge can be treated as a nearly flat film on the solid surface with Poiseuille-type flow with (1) a slip length of $-U_{ls}$ (frame of reference moving with the liquid) (2) a no-shear BC at liquid/vapor interface (3) an average velocity of zero at steady state (droplet has reached the equilibrium state) (**Figure 4.4.C**) [79, 81]:

$$v(h) = U_{ls}(\frac{1}{2} - \frac{3}{2}(\frac{h_0 - h}{h_0})^2) \qquad \text{Eq. (22)}$$

where $-U_{ls}$ is the velocity of the liquid at the solid-liquid boundary and h_0 is the height corresponding to the maximum velocity. The viscous dissipation, ξ, of the fluid flow is related to the viscous force, F_v, and the velocity profile, $v(h)$, by [79, 82]:

$$\xi = F_v U_{ls} \qquad \text{Eq. (23a)}$$

$$\xi \sim R \int_0^{h_0} \eta (\frac{dv}{dh})^2 dh \qquad \text{Eq. (23b)}$$

$$\frac{F_v}{l} \sim \frac{\eta U_{ls} r}{h_0} \qquad \text{Eq. (23c)}$$

For a spherical cap of constant volume, $\theta_d \sim h_0/r$ and $h_0 \sim V/r^2$. Since the droplet is an incompressible fluid, $V \sim R^3$, where R is the radius of the initial droplet. When the droplet is spreading, **Equation 21** and **Equation 23c** are balanced and the radius of the wetted area, r_{cap}, scales as:

$$r_{cap} \sim R\left(\frac{\gamma\tau}{\eta R}\right)^{1/10} \qquad \text{Eq. (24)}$$

Since Tanner was the first to experimentally observe this power law dependence for the spreading of liquid droplets in air, **Equation 24** is often called Tanner's law [75-77].

For systems that cannot be described using Tanner's law, spreading is described using a general power law that is not based on any theory:

$$r_{cap} = k\tau^n \qquad \text{Eq. (25)}$$

where k and n are system-dependent. Experimentally, surface roughness strongly influences n, particularly for low viscosity liquids spreading in air and liquids spreading in the presence of an external liquid [83]. For drops with a Bond number Bo < 1, the capillary regime can describe spreading behavior until the droplet reaches equilibrium [76]. The original premise of near perfect wetting and negligible shear stress at the droplet/fluid interface for the capillary regime suggests severe limitations to its applicability in practical solutions. It has nonetheless been used successfully to describe wetting kinetics in liquid/vapor systems for cases of equilibrium contact angles up to 70^o [84]. Given the non-zero viscosity of the surrounding liquid for the liquid/liquid systems examined in this study, we would not expect the droplet to spread with a $t^{1/10}$ dependence in the slower spreading regime.

4.2 Methods

The effect of surface roughness, wetting order, and fluid system were examined using the same systems used in equilibrium wetting behavior studies. The relevant liquid properties are listed in **Table 1**.

High speed video microscopy was used to capture spreading behavior on surfaces with variable roughness. Videos were captured using a Phantom v7.1 high speed camera at a frame rate of 1000 – 2000 fps, for 1 s. The spreading behavior of sessile water droplets in decane and air required a frame rate of 2000 fps to capture spreading behavior in the inertial regime. The high speed camera was mounted to a Nikon TE2000-E inverted microscope to capture spreading behavior of sessile water droplets (**Figure 4.5.A** and **Figure 4.5.C**) and to a Nikon Eclipse 50i upright microscope to capture spreading behavior of inverted oil droplets (**Figure 4.5.B** and **Figure 4.5.D**).

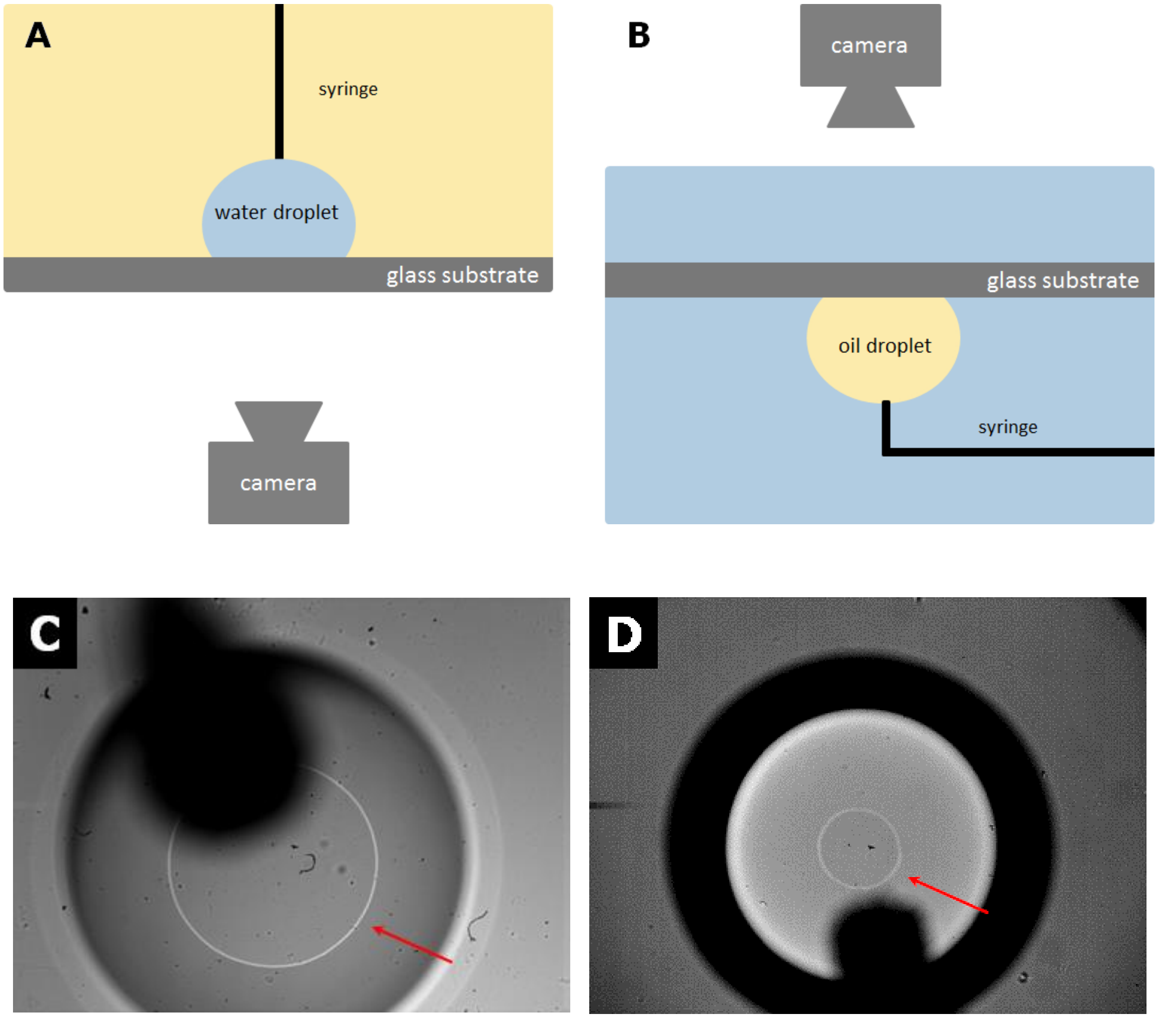

Figure 4.5. (A) Spreading of sessile water droplet in oil was measured using an inverted microscope and (B) spreading of an inverted oil droplet in water was measured using an upright microscope. (C) and (D) represent an image of a spreading droplet from each set up. The wetted area is indicated with a red arrow.

Droplets were formed using a syringe pump (New Era Pump Systems Inc., NE-300) and grown at a rate of 5 µL/min so impact velocity effects could be neglected [69]. Liquid droplets were small enough that Bo < 1 and gravitational effects could be ignored. Each recorded measurement is the average of at least three droplets.

Videos of the spreading process were converted into TIFF files using Phantom Camera Control (PCC) software by Vision Research Inc. Spreading in liquid/liquid systems was captured using bright field microscopy. The traditional method was not able to capture the spreading behavior of water droplets in air. Reflection interference microscopy was used for that system.

4.2.1 Reflection interference contrast microscopy

When the spreading of a sessile water droplet in air was imaged using bright field microscopy, the light reflected off the needle and the water droplet in such a way that it made it impossible to determine when the droplet made contact with the surface (**Figure 4.6**).

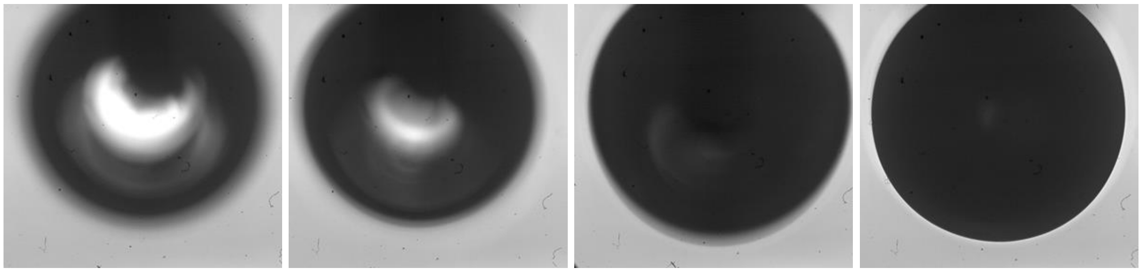

Figure 4.6. Bright field images of a sessile water droplet over the course of 10 ms

In order to overcome this challenge, sessile water droplet experiments were performed using reflection interference contrast microscopy (RICM). Unlike bright field microscopy (**Figure 4.7.A**), where the stage is illuminated from above, RICM illuminates the stage from below. In this study, RICM was achieved using a white light source, two linear polarizers, and a 50% mirror. White light (Nikon Intensilight, C-HGFIE) passed through a polarizer before it was first reflected off a 50% mirror onto the stage. Reflected light from the sample then passed through the mirror into the camera. The second polarizer was placed underneath the mirror to filter out any stray light (**Figure 4.7.B**).

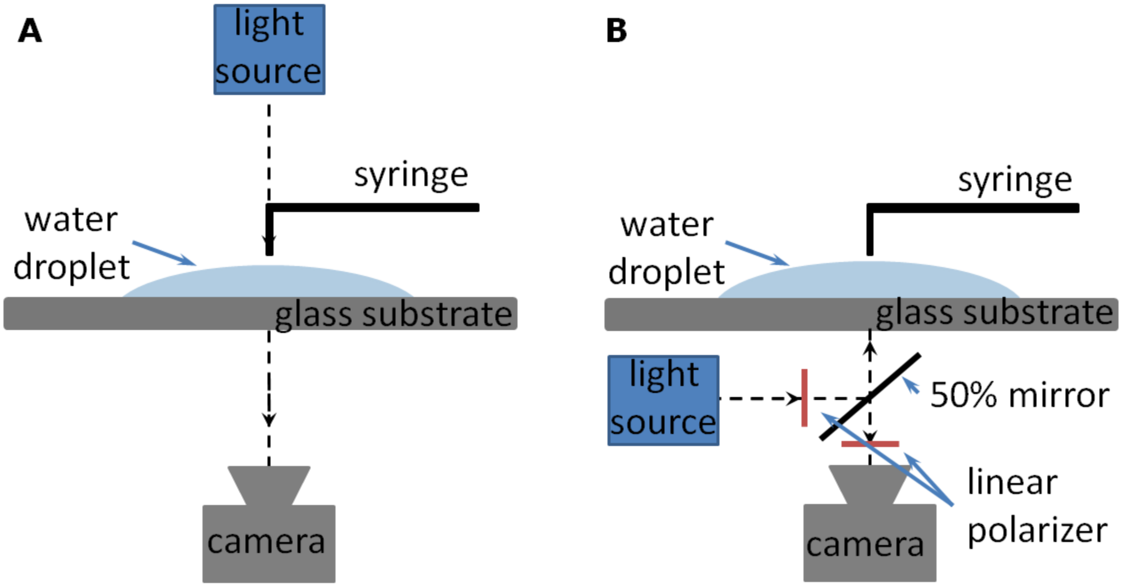

Figure 4.7. Comparison of microscope set-up using (A) bright field microscopy and (B) RICM

The principle of RICM is depicted in **Figure 4.8.A** [85, 86]. Light illuminates the stage from below with an intensity I_0. The light is partially reflected at the glass/air interface and now has intensity I_1. The glass/air reflection is relatively strong, which results in a relatively bright background. The presence of water on the glass will modify the background reflection. Since the refractive index of water is higher than air, the intensity of the reflected light, I_4, will be lower than I_1. Near the contact line, light that will reflect at both the water/air (I_2) and water/glass interface (I_3). The reflected light will be a superposition of the two intensities. The reflected light near the interface will be out of phase, resulting in light or dark fringe patterns near the contact line. An example of the fringe pattern can be seen in **Figure 4.8.B**. Since the monochromatic light used for RICM was not collimated, the fringe pattern is not very clear.

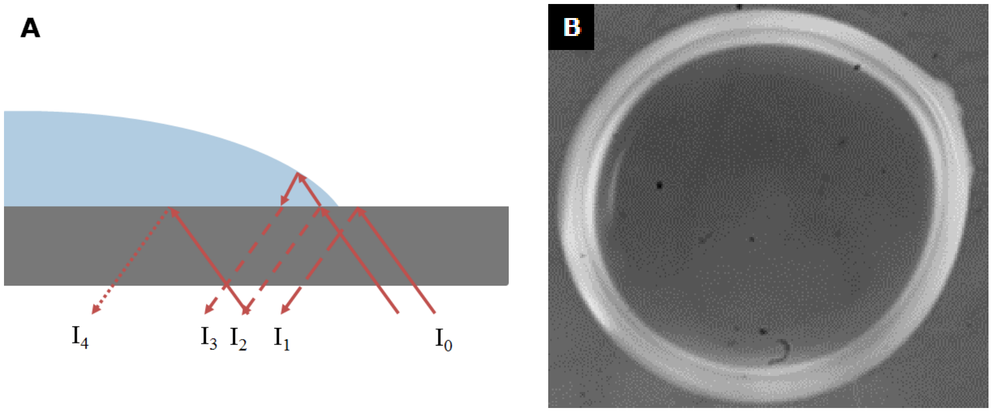

Figure 4.8. Basic principle of RICM. (A) Light illuminates the sample from below with intensity I_0 (solid arrows). Light can be reflected at the air/glass interface (I_1) or the glass/water interface (I_4). Because of the different indices of refraction, the intensity of reflected light will be different. Near the contact line of the droplet, light can be reflected both at the water/glass (I_2) and the water/air interface (I_3). The intensity of light is then the superposition of I2 and I3. There will be a phase shift between the two light paths, resulting in the appearance of either light or dark "fringes". (B) Fringes can be seen near the edge of a water droplet on untreated glass.

RICM can only produce a fringe pattern if the water/air interface is several microns above the glass. For the purposes of this study, the use of RICM was only to elucidate the boundary of the wetted area (**Figure 4.9**).

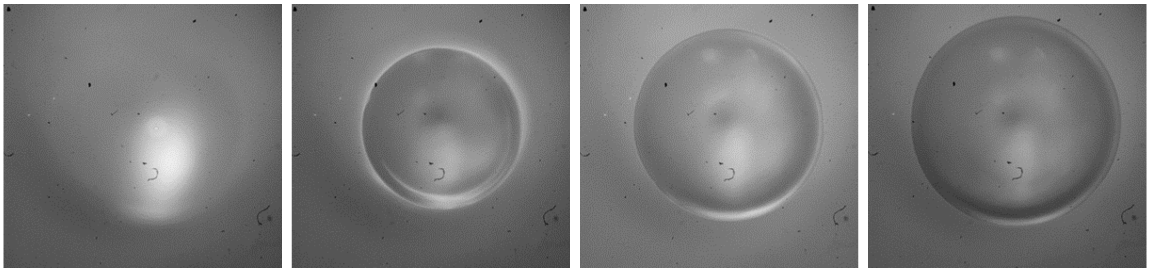

Figure 4.9. Evolution of the wetted area for a water droplet on a rough substrate at (A) -0.5 ms, (B) 250 ms, (C) 500 ms, and (D) 1000 ms after contact with the solid surface

Images from the experiments were then analyzed to determine the radius of the wetted area as a function of time.

4.2.2 Data analysis

All droplets were assumed to be spherical and incompressible at the time of contact. The radius of droplet during the time of contact (*R*) could then be determined using the volume of a sphere. Custom MATLAB scripts were used to determine the radius of the wetted area. An example is shown in **Figure 4.10**.

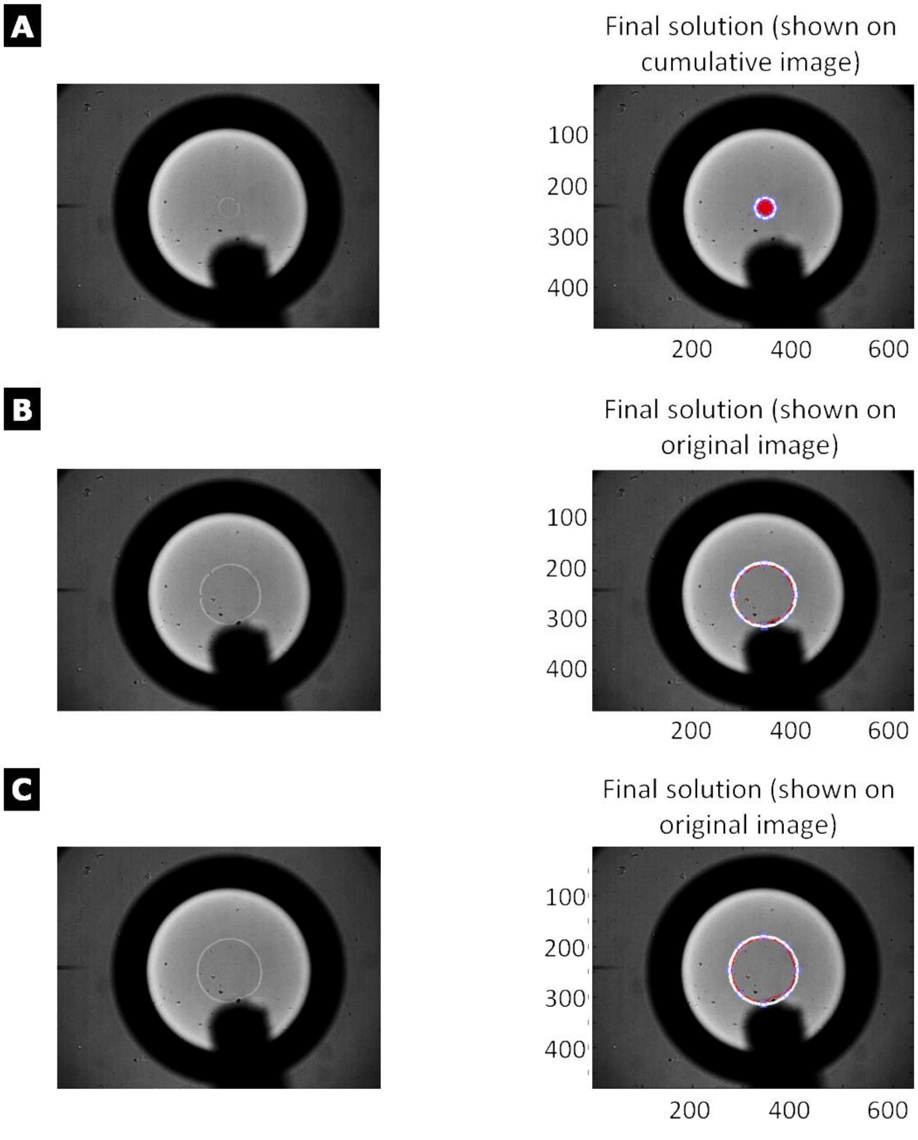

Figure 4.10. Determination of the radius of the wetted area of a decane droplet spreading in water at (A) 20 ms, (B) 500 ms, and (C) 1000 ms after the droplet contacted the surface. The axes refer to the number of pixels in the image in the *x* and *y* direction.

The data were fit to determine the observable spreading regimes using OriginPro® v 8.6. Error bars were not included for clarity. The extent of droplet spreading was characterized by the non-dimensionalized radius of the wetted area (r/R).

4.3 Results

Droplet spreading has traditionally been examined within the framework of liquid/vapor systems with varying liquid viscosity. An increase in drop viscosity generally delays the transition from the inertial spreading stage ($r \sim t^{1/2}$) to the capillary stage ($r \sim t^{1/10}$) [70]. A similar trend can be seen in liquid/liquid systems, where an increase in the viscosity of the surrounding liquid results in a delayed transition between a fast spreading regime and a slow spreading regime (**Figure 4.11**).

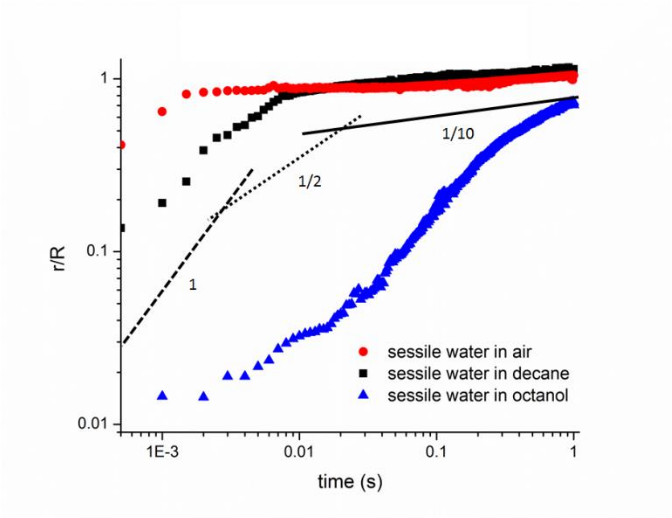

Figure 4.11. Spreading of a sessile water drop on the smoothest surface (4.66 nm rms roughness, 60% acetone treatment) in air (●), decane (■), and octanol (▲). Lines were drawn to guide the eye. Dotted, dashed, and solid lines represent an $r{\sim}t$ (viscous regime), $r{\sim}t^{1/2}$ (inertial regime), and $r{\sim}t^{1/10}$ (capillary regime) dependence, respectively

The relatively slow spreading rate in the octanol/water system compared to the decane/water and water/air system was also seen when equilibrium contact angle measurements were made using the static contact angle method, though the characterization of spreading time was much less precise (**Section 3.2.1**). The droplets in the water/octanol system took much longer to relax to an assumed equilibrium state than droplets in the decane/water or the water/air systems.

Theoretical descriptions of droplet spreading divide the fast regime into the viscous and inertial regimes, each with a different characteristic dependence on time. For the fluid/fluid systems studied here, it was difficult to determine the exact transition between the viscous and inertial regimes. The two were therefore combined and called the "visco-inertial" spreading regime, characterized by a radial dependence on time ranging from $t^{1/2}$ to t.

Traditionally, the visco-inertial regime has only been observed in the ms range if the spreading liquid was extremely viscous (η > 10 mPa s) [70, 73]. The results suggest that spreading kinetics for low viscosity liquids can be significantly retarded in the presence of an external liquid.

4.3.1 Air/water system

For a sessile water droplet, the duration of the inertial regime is approximately 1 ms [23]. Due to experimental limitations, only the capillary regime was observed in this study. Increasing the surface roughness corresponded to an increase in the droplet spreading rate, which is similar to behavior seen in other liquid/vapor systems (**Figure 4.12**) [17, 20, 22, 24, 69, 70].

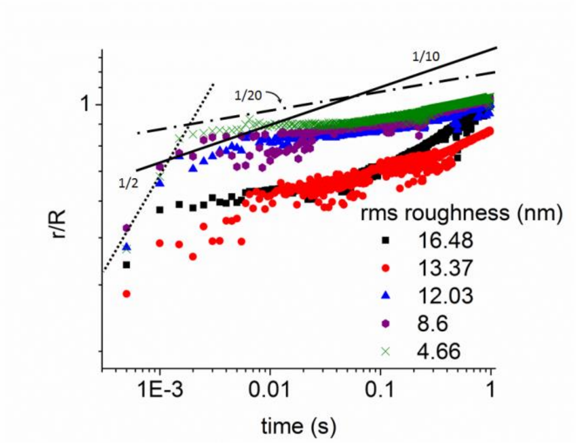

Figure 4.12. Spreading of a sessile water drop in air. Lines were drawn to guide the eye. Dotted, solid, and dot-dash lines represent an $r \sim t^{1/2}$, an $r \sim t^{1/10}$, and an $r \sim t^{1/20}$ dependence.

The exact rate of spreading for the water droplets in air is unclear. However, there is a clear roughness-dependent transition, with a faster spreading rate on rougher substrates. From SEM images, this threshold roughly corresponds to a change in the shape of the surface asperities from discrete particles with overhanging parts to wavy roughness features (**Figure 2.4**).

A slower spreading rate is generally associated with a higher equilibrium contact angle [17, 22, 70]. The equilibrium contact angles for smooth and rough substrates in the water/air system are approximately the same (**Figure 3.11**). The results suggest that for ES100 polymer substrates, surface roughness only affects dynamic wetting behavior.

4.3.2 Decane/water systems

When the primary wetting fluid is liquid, spreading dynamics slows sufficiently to observe multiple spreading regimes (**Figure 4.13**). For both decane/water systems, spreading is characterized first by a fast regime and a slow one. The transition between the two regimes appears to be dependent on the surface roughness, but is much more obvious when water is the primary wetting liquid. The order the liquids are introduced to the solid clearly affects early spreading behavior (**Figure 4.13.B**).

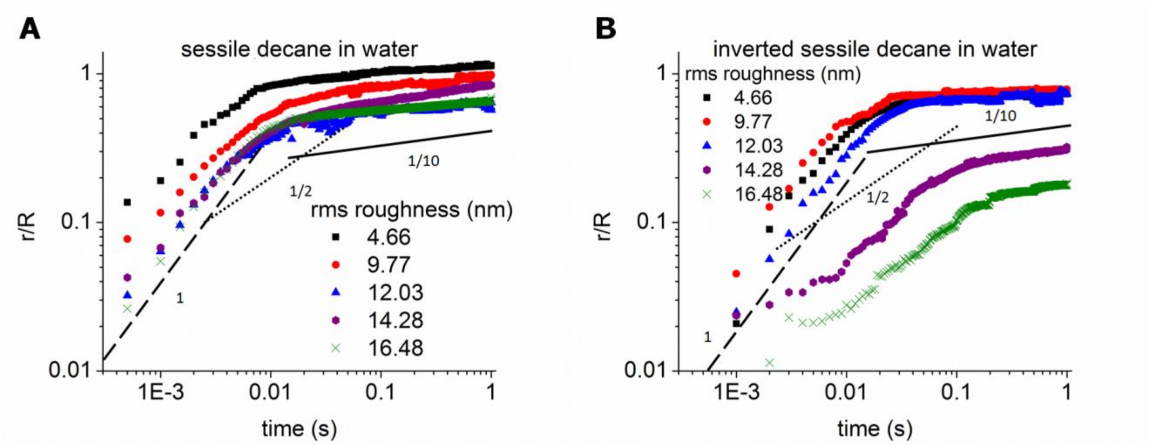

Figure 4.13. Spreading of (A) a sessile water drop in decane and (B) an inverted sessile decane drop in water. Lines were drawn to guide the eye. The dotted, dashed, and solid line represent an $r \sim t$, $r \sim t^{1/2}$, and $r \sim t^{1/10}$ dependence, respectively.

The roughness-dependent transitions between the three regimes appear to be unique to liquid/liquid systems, since this type of wetting behavior has not been seen in liquid/vapor systems. In liquid/vapor systems, the duration of the viscous and inertial regimes has usually been attributed to differences in liquid properties and not to surface wettability [22, 69, 70]. The viscosity of the surrounding fluid clearly affects droplet spreading behavior by making it more sensitive to surface roughness, but the exact dependence is still unclear.

When decane was the primary wetting liquid (**Figure 4.13.A**), there was no systematic dependence of spreading rate in the slow spreading regime on rms roughness, which suggests that surface roughness has no effect on spreading behavior in the capillary regime. In liquid/vapor systems with very viscous liquids, the spreading rate in the capillary regime increased with decreasing equilibrium contact angle, θ_{eq}, on chemically heterogeneous, smooth surfaces and increased significantly with increasing surface roughness on roughened glass surfaces [70, 83]. Given that θ_{eq} for sessile water droplets in decane shows a systematic dependence on surface roughness (**Figure 3.14**), and the spreading rate does not have the same dependence, it is possible that the external fluid affects the spreading rate in the slow regime.

The presence of an external liquid and the low viscosity of the primary and secondary liquids seem to affect spreading behavior in both the visco-inertial and capillary regimes, given that the observed behavior is so different than what has been observed for liquid/vapor systems. To date, there are no theories designed to cover the two-liquid systems in this study.

4.3.3 Octanol/water systems

In the octanol/water system with octanol as the primary wetting liquid, the overall spreading rate was so slow that the it was difficult to determine if the droplet ever reached the capillary regime (**Figure 4.14.A**). When a water droplet was placed on surfaces with an rms roughness of 12.50 nm and 14.28 nm, the spreading in the first second was very limited. The observed behavior was expected, considering the equilibrium droplet contact angle for those surfaces was $\geq 150^o$ (**Figure 3.16**) [87]. The spreading behavior for substrates in the octanol/water system with water as the primary wetting liquid was faster that the system with the opposite wetting order (**Figure 4.14.B**), which suggests that wetting order affects the spreading rate in liquid/liquid systems regardless of the polarity of the non-aqueous liquid.

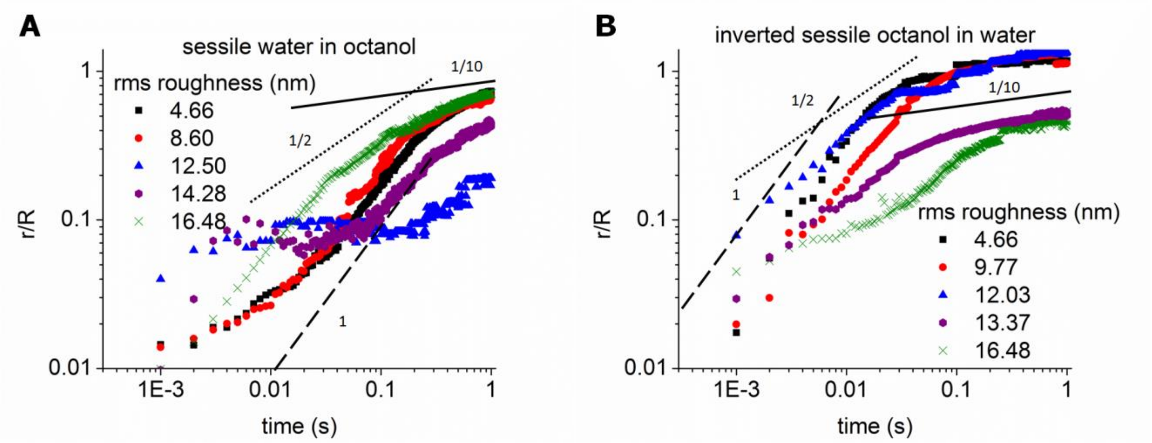

Figure 4.14. Spreading of (A) a sessile water drop in octanol and (B) an inverted sessile octanol drop in water. Lines were drawn to guide the eye. The dotted, dashed, and solid line represent an $r \sim t$, $r \sim t^{1/2}$, and $r \sim t^{1/10}$ dependence, respectively

In both octanol/water systems, the observed spreading behavior correlates with equilibrium wetting behavior: the overall spreading rate is slower for substrates with a higher droplet equilibrium contact angle. The slow spreading regime is only observed when water is the primary wetting liquid, although the transition from the visco-inertial regime to the capillary regime is unclear. In that system, it appears that surface roughness does not affect the spreading rate within the slow regime.

The spreading rate in the visco-inertial regime for both decane/water and octanol/water systems are influenced by surface roughness. This is very different than spreading behavior in liquid/vapor systems, where spreading in the visco-inertial regime has been shown to only depend on liquid properties [23, 69]. In liquid/liquid systems, the surrounding liquid and the surface roughness must play some role in early spreading behavior.

4.4 Concluding remarks

This study was the first to isolate the effects of surface roughness in spreading behavior for low viscosity liquid/liquid systems. Spreading behavior was determined using a combination of bright field and reflection interference contrast microscopy. Experimentally, videos of droplets spreading were captured using a high speed camera and then converted into image files to extract the radius of the wetted area. Spreading rates were characterized by the change in the wetted area as a function of time.

In general, varying the surface roughness had little to no effect in changing the spreading rate during the capillary regime. Changing the surface roughness did have an overall effect on the spreading rate because it delayed transition between the different spreading regimes. The exact dependence on surface roughness is still unknown and needs to be further studied. For both liquid/liquid systems, the wetting order clearly influenced spreading behavior, particularly during the visco-inertial regime.

Many of the characteristic time scales used to describe spreading behavior were determined empirically using liquid/vapor systems where the liquid was extremely viscous. Since this work is the first to present data of droplet spreading dependent only on surface roughness, future work will include determining how the surface affects different transition times, particularly between the viscous and inertial regime, where there has not been much research in liquid/liquid systems. This work also only examined the first second after a droplet touched the surface. In order to compare this work to others using the molecular kinetic theory to describe spreading in liquid/liquid systems, longer experimental times must be used.

CHAPTER 5

CONCLUSIONS AND RECOMMENDATIONS

Solid surface wettability in fluid/fluid systems is of interest in many applications. This study is the first that isolates the effect of surface roughness for different fluid/fluid systems to examine its role in both equilibrium and dynamic wetting behavior.

The solid surfaces used in this study consisted of polymer-coated glass with varying roughness. Unlike traditional methods, the substrates used in this study were generated in a way that controlled both surface topography and chemistry. Polymer particles were generated using a block co-polymer with negatively charged functional groups dispersed throughout the polymer chain, which resulted in chemically homogeneous particles. Rough surfaces were prepared through the irreversible adsorption of the negatively charged polymer particles onto positively functionalized glass. Once rough substrates were generated, a solvent-based smoothing procedure was used to very slowly partially dissolve the particles and redeposit free polymer back to the exposed surface. Scanning electron microscopy (SEM) and atomic force microscopy (AFM) were used to verify a successful change of the surface topography. X-ray photoelectron spectroscopy (XPS) and electrokinetic analysis (EKA) were used to verify if the original surface chemistry was retained. Solid surface energy parameters were determined using the vOCG method.

Wetting behavior was determined using three fluid/fluid systems: air/water, decane/water, and octanol/water. Equilibrium wetting behavior was characterized via contact angle measurements. Regardless of wetting order, the inherent wettability of solid surfaces is influenced by the reference fluids. Substrates that were hydrophilic in an air/water system appeared equiphilic in a decane/water system, and unambiguously hydrophobic in an octanol/water system. Similarly, increasing the surface roughness always resulted in a Cassie state. However, effects of the three influencing factors (fluid polarity, wetting order, and surface roughness) appear coupled in a non-trivial manner: in the octanol/water system, only when water is the primary wetting liquid can we tell for sure that a transition from Wenzel to Cassie-Baxter wetting occurs. The system- and order-dependent transition was verified using a modified Wenzel/Cassie-Baxter model.

Dynamic wetting behavior of liquid droplets was determined using bright field microscopy and reflection interference contrast microscopy (RICM). Droplet spreading was captured using a high speed camera, and images were processed to extract the change in the wetted area with respect to time. The effects of surface roughness, wetting order, and reference system were examined. Using an oil/water system slowed droplet spreading significantly to the point where it was possible to observe the initial visco-inertial regime, which has not been studied systematically in liquid/liquid systems, particularly for liquids with low viscosities. The length of the visco-inertial regime increased with increasing substrate roughness and oil viscosity. Regardless of surface roughness, spreading is roughly consistent with the $t^{1/10}$ scaling predicted for highly wetting drops in air and does not appear to depend strongly on surface roughness. Both behaviors are unexpected when compared to spreading behavior in liquid/vapor systems. Systems characterized by high equilibrium contact angles also exhibited a delayed onset of the visco-inertial spreading regime.

This study examined the effect of surface roughness for substrates coated with 60 nm ES100 polymer particles. By using larger particles or substrates coated with a hydrophobic polymer, it would be possible to determine the universality of the observed wetting behavior.

Decane and octanol were chosen based on their different dielectric constants and ES-100 insolubility. Diiodomethane is another solution that ES100 is insoluble in and has a dielectric constant between that of decane and octanol. Using diiodomethane as another reference liquid would provide a more complete picture on the dependence of wetting behavior on relative liquid polarity and viscosity.

There are currently no theories that adequately describe spreading behavior in liquid/liquid systems during the viscous, inertial, and capillary regimes. The results indicate that theories derived for liquid/vapor systems are not applicable for liquid/liquid systems. This study will be useful in guiding modeling efforts to better understand spreading in liquid/liquid systems, particularly how surface roughness affects droplet spreading in the viscous and inertial stages. Furthermore, the results detailed here can be used to determine the characteristic times and relevant constants associated with different spreading regimes in liquid/liquid systems.

This study examined several ways in which fluid/liquid/solid interactions are influenced by surface roughness. A related area of research is the examination of solid/solid interactions between two rough surfaces in a liquid medium, the most common model system being the interaction between a particle and a solid surface in water. This configuration is used to describe a multitude of processes, such as membrane-based separation and surface contamination [30, 88, 89]. Despite its ubiquity, there is no standard theory to describe interactions between rough solid surfaces in water [88-90]. There is also a lack of experimental evidence to verify existing theoretical predictions because most well-characterized surfaces have simultaneously varying surface chemistry and topography.

The substrate fabrication method used in this study varied surface topography while retaining the original surface chemistry and can be easily applied to the modification of spherical particles [27]. Furthermore, the thorough characterization of the solid surface as well as the roughness-dependent solid/liquid interactions determined in this study will be useful in determining the effect of surface roughness in solid/solid interactions in a liquid medium.

REFERENCES

1. Quéré, D., *Annu Rev Mater Res*, 2008. **38**(1): p. 71-99.
2. Morrow, N.R., *J Can Pet Technol*, 1975. **14**(04).
3. Shaker Shiran, B. and A. Skauge, *Energ Fuel*, 2013. **27**(3): p. 1223-1235.
4. Cheng, Q., et al., *Soft Matter*, 2012. **8**(25): p. 6740-6743.
5. Tang, G.-Q. and N.R. Morrow, *J Petrol Sci Eng*, 1999. **24**(2–4): p. 99-111.
6. Yin, X., et al., *J Mater Chem A*, 2014. **2**(16): p. 5620-5624.
7. Kobayashi, M., et al., *Langmuir*, 2012. **28**(18): p. 7212-7222.
8. Yang, W.J., et al., *Biofouling*, 2012. **28**(9): p. 895-912.
9. Morrow, N.R. and G. Mason, *Curr Opin Colloid Interface Sci*, 2001. **6**(4): p. 321-337.
10. Nosonovsky, M., & Rohatgi, P. K., *Biomimetics in materials science*. 2012, Springer: New York. p. 343-354.
11. Jung, Y.C. and B. Bhushan, *Langmuir*, 2009. **25**(24): p. 14165-14173.
12. Kang, H.C. and A.M. Jacobi, *Langmuir*, 2011. **27**(24): p. 14910-14918.
13. Zhang, X., et al., *Surf Rev Lett*, 2004. **11**(1): p. 7-13.
14. Meiron, T.S., A. Marmur, and I.S. Saguy, *J Colloid Interface Sci*, 2004. **274**(2): p. 637-644.
15. Marmur, A., *Contact Angle Wettability and Adhesion*, 2009. **6**(3).
16. Prabhu, K.N., P. Fernades, and G. Kumar, *Mater Design*, 2009. **30**(2): p. 297-305.
17. McHale, G., et al., *Phys Rev Lett*, 2004. **93**(3): p. 036102.
18. Li, L., V. Breedveld, and D.W. Hess, *ACS Appl Mater Interfaces*, 2013. **5**(11): p. 5381-5386.
19. Ramiasa, M., et al., *J Phys Chem C*, 2012. **116**(20): p. 10934-10943.
20. Snoeijer, J.H. and B. Andreotti, *Annu Rev Fluid Mech*, 2013. **45**(1): p. 269-292.
21. Fries, N. and M. Dreyer, *J Colloid Interface Sci*, 2008. **327**(1): p. 125-128.

22. Bird, J.C., S. Mandre, and H.A. Stone, *Phys Rev Lett*, 2008. **100**(23): p. 234501.

23. Biance, A.-L., C. Clanet, and D. Quéré, *Phys Rev E: Stat Phys, Plasmas, Fluids*, 2004. **69**(1): p. 016301.

24. Paulsen, J.D., J.C. Burton, and S.R. Nagel, *Phys Rev Lett*, 2011. **106**(11): p. 114501.

25. Duchemin, L., J. Eggers, and C. Josserand, *J Fluid Mech*, 2003. **487**: p. 167-178.

26. Seveno, D., et al., *Langmuir*, 2011. **27**(24): p. 14958-14967.

27. San-Miguel, A. and S.H. Behrens, *Langmuir*, 2012. **28**(33): p. 12038-12043.

28. San Miguel, A., et al., *Soft Matter*, 2010. **6**(14): p. 3163-3166.

29. Vitale, S.A. and J.L. Katz, *Langmuir*, 2003. **19**(10): p. 4105-4110.

30. Hoek, E.M.V., S. Bhattacharjee, and M. Elimelech, *Langmuir*, 2003. **19**(11): p. 4836-4847.

31. Gadelmawla, E., et al., *J Mater Process Technol*, 2002. **123**(1): p. 133-145.

32. Wysocka, K., et al., *Optica Applicata*, 2008. **38**(1).

33. Yasuda, E.-i., *Carbon alloys: novel concepts to develop carbon science and technology*. 2003: Gulf Professional Publishing.

34. d'Agostino, R., et al., *Plasma Processes and Polymers-16th International Symposium on Plasma Chemistry*. Taornina, Italy: Wiley-VCH. 2005.

35. Hunter, R.J., *Zeta potential in colloid science: principles and applications*. Vol. 8. 1981: Academic press London.

36. Schnitzer, C. and S. Ripperger, *Chem Eng Technol*, 2008. **31**(11): p. 1696-1700.

37. Schwarz, J.A. and C.I. Contescu, *Surfaces of nanoparticles and porous materials*. 2002: CRC Press.

38. Wu, Z., et al., *J Colloid Interface Sci*, 2006. **304**(1): p. 119-124.

39. Buk, H., *Acta Chim Slov*, 2010. **57**: p. 700-706.

40. Kenny, D.A., *Statistics for the social and behavioral sciences*. 1987: Little, Brown Boston.

41. Elimelech, M., W.H. Chen, and J.J. Waypa, *Desalination*, 1994. **95**(3): p. 269-286.

42. Young, T., *Phil Trans R Soc London*, 1805: p. 65-87.

43. Wenzel, R.N., *Ind Eng Chem*, 1936. **28**(8): p. 988-994.

44. Cassie, A.B.D. and S. Baxter, *Trans Faraday Soc*, 1944. **40**(0): p. 546-551.

45. Fowkes, F.M., *J Adhes Sci Technol*, 1987. **1**(1): p. 7-27.

46. Van Oss, C.J., *Interfacial forces in aqueous media*. 2006: CRC press.

47. Fowkes, F.M., *J Phys Chem*, 1963. **67**(12): p. 2538-2541.

48. Van Oss, C., R. Good, and M. Chaudhury, *J Colloid Interface Sci*, 1986. **111**(2): p. 378-390.

49. Van Oss, C.J., M.K. Chaudhury, and R.J. Good, *Chem Rev*, 1988. **88**(6): p. 927-941.

50. Van Oss, C., et al., *J Colloid Interface Sci*, 1989. **128**(2): p. 313-319.

51. Schrader, M.E., *Langmuir*, 1995. **11**(9): p. 3585-3589.

52. Freitas, A.A., F.H. Quina, and F.A. Carroll, *J Phys Chem B*, 1997. **101**(38): p. 7488-7493.

53. Korhonen, J.T., et al., *Langmuir*, 2013. **29**(12): p. 3858-3863.

54. Marmur, A., *Soft Matter*, 2006. **2**(1): p. 12-17.

55. Cwikel, D., et al., *Langmuir*, 2010. **26**(19): p. 15289-15294.

56. Decker, E., et al., *Colloids Surf, A*, 1999. **156**(1): p. 177-189.

57. Andrieu, C., C. Sykes, and F. Brochard, *Langmuir*, 1994. **10**(7): p. 2077-2080.

58. Rodriguez-Valverde, M.A., F.J.M. Ruiz-Cabello, and M.A. Cabrerizo-Vilchez, *Soft Matter*, 2011. **7**(1): p. 53-56.

59. Ruiz-Cabello, F.J.M., M.A. Rodríguez-Valverde, and M.A. Cabrerizo-Vilchez, *J Adhes Sci Technol*, 2011. **25**(16): p. 2039-2049.

60. Lam, C.N.C., et al., *Adv Colloid Interface Sci*, 2002. **96**(1–3): p. 169-191.

61. Żenkiewicz, M., *JAMME*, 2007. **24**(1): p. 137-145.

62. Van Oss, C., *Interfacial forces in aqueous media*. New York: Marcel Dekker, Inc. 1994.

63. Gooch, J.W., *Encyclopedic dictionary of polymers*. Vol. 1. 2010: Springer.

64. He, Y., et al., *Appl Surf Sci*, 2011. **257**(17): p. 7689-7692.

65. Bellanger, H., et al., *Chem Rev*, 2014. **114**(5): p. 2694-2716.

66. Papadopoulos, P., et al., *PNAS*, 2013. **110**(9): p. 3254-3258.

67. McHale, G., M.I. Newton, and N.J. Shirtcliffe, *Eur J Soil Sci*, 2005. **56**(4): p. 445-452.

68. Zhang, L., et al., *Chem Mater*, 2007. **19**(4): p. 948-953.

69. Stapelbroek, B., et al., *Soft Matter*, 2014. **10**(15): p. 2641-2648.

70. Eddi, A., K.G. Winkels, and J.H. Snoeijer, *Phys Fluids*, 2013. **25**(1): p. 013102.

71. Hopper, R.W., *J Fluid Mech*, 1990. **213**: p. 349-375.

72. Eggers, J., J.R. Lister, and H.A. Stone, *J Fluid Mech*, 1999. **401**: p. 293-310.

73. Seveno, D., et al., *Langmuir*, 2009. **25**(22): p. 13034-13044.

74. Seaver, A.E. and J.C. Berg, *J Appl Polym Sci*, 1994. **52**(3): p. 431-435.

75. Tanner, L., *J Phys D: Appl Phys*, 1979. **12**(9): p. 1473.

76. Cazabat, A.M. and M.A.C. Stuart, *J Phys Chem*, 1986. **90**(22): p. 5845-5849.

77. Cox, R.G., *J Fluid Mech*, 1983. **131**: p. 1--26.

78. Huh, C. and L. Scriven, *J Colloid Interface Sci*, 1971. **35**(1): p. 85-101.

79. de Gennes, P.-G., *Colloid Polym Sci*, 1986. **264**(5): p. 463-465.

80. Kirkinis, E. and S. Davis, *Phys Rev Lett*, 2013. **110**(23): p. 234503.

81. De Gennes, P.-G., *Rev Mod Phys*, 1985. **57**(3): p. 827.

82. Bico, J. and D. Quéré, *J Colloid Interface Sci*, 2001. **243**(1): p. 262-264.

83. Apel-Paz, M. and A. Marmur, *Colloids Surf, A*, 1999. **146**(1): p. 273-279.

84. Fermigier, M. and P. Jenffer, *J Colloid Interface Sci*, 1991. **146**(1): p. 226-241.

85. Rädler, J. and E. Sackmann, *J Phys II* 1993. **3**(5): p. 727-748.

86. Verschueren, H., *J Cell Sci*, 1985. **75**(1): p. 279-301.

87. Barthlott, W. and C. Neinhuis, *Planta*, 1997. **202**(1): p. 1-8.

88. Huang, X., S. Bhattacharjee, and E.M. Hoek, *Langmuir*, 2009. **26**(4): p. 2528-2537.

89. Bitter, J.L., et al., *Langmuir*, 2013. **29**(28): p. 8835-8844.

90. Suresh, L. and J.Y. Walz, *J Colloid Interface Sci*, 1996. **183**(1): p. 199-213.